This manuscript has been accepted for publication in JGR: Solid Earth This version is not yet published and may differ from the publication version.

3D dynamic rupture modeling of the 2021 Haiti earthquake used to constrain stress conditions and fault system complexity

H. Zoe Yin¹, Mathilde Marchandon², Jennifer S. Haase¹, Alice-Agnes Gabriel^{1,2}, Roby Douilly ³

¹Scripps Institution of Oceanography, UCSD, La Jolla, CA, USA
²Department of Earth and Environmental Sciences, Ludwig Maximilian University of Munich, Munich,

Germany
³University of California, Riverside, CA, USA

Key Points:

10

12

13

15

- Dynamic rupture modeling shows that regional stress shape, orientation, and fault geometry are key controls on the 2021 Haiti rupture.
- Regional stress shape and orientation may be highly variable within the southern peninsula of Haiti.
- Geometric complexity plays a large role in ongoing rupture segmentation of Haiti's southern peninsula.

Corresponding author: Jennifer S. Haase, jhaase@ucsd.edu

Abstract

18

19

20

22

23

24

25

26

27

28

30

31

32

33

34

35

36

38

30

40

41

42

43

45

46

47

49

50

52

53

54

55

57

58

59

60

61

65

66

The 2021 M_w 7.2 Haiti earthquake was a devastating event which occurred within the Enriquillo Plantain Garden Fault Zone (EPGFZ). It is not well-understood why neither the 2021 nor the prior 2010 M_w 7.0 earthquakes were pure strike slip events and, instead, ruptured with distinct patches of dip slip and strike slip motion on largely separate fault planes. The major characteristics of the earthquake rupture include: the characteristic spatial and temporal separation of strike-slip and dip-slip motion, rupture transfer to the Ravine du Sud Fault (RSF), and a multi-peak source time function. We develop several 3D dynamic rupture simulations of the 2021 earthquake to analyze which conditions may have controlled the complex rupture. We construct a detailed fault system geometry with 17 fault segments, including a north-dipping Thrust Fault (TF) and near-vertical RSF, along with surrounding regional and secondary faults. We find that along-strike changes to the frictional strength of the TF are needed to focus the slip to match the scale and pattern of surface deformation observed with InSAR. Lateral changes in the regional stress shape and orientation are key to generating the observed rupture transfer from the TF to the RSF while maintaining the rake required to match the broad In-SAR surface deformation pattern and multi-peak source time function. The dynamic rupture modeling results suggest that significant variability in fault stress and strength as well as complexities of the subsurface geometry may have been key controlling factors on the dynamics of the 2021 rupture.

Plain Language Summary

The southern peninsula of Haiti experiences high seismic hazard and has endured catastrophic impacts from past major earthquakes, most notably the 2010 M_w 7.0 earthquake which was one of the deadliest earthquakes recorded globally. In 2021, a M_w 7.2 earthquake killed over 2000 people and underlined the importance of better understanding the hazardous Enriquillo Plantain Garden Fault Zone (EPGFZ) which produced both of these destructive events. Both events were considerably more complex than was previously thought to be typical based on the geologic record and raise interesting questions about what conditions drive earthquake ruptures in this region. In this study, we develop numerical models (i.e. dynamic rupture models) of the 2021 earthquake which explore which conditions may have driven the observed rupture characteristics. We find that the the accumulation of stress on the fault planes likely has large variability and, along with fault geometry and strength complexity, may have contributed to the observed 2021 rupture. These findings have implications for characterizing seismic hazard in this region.

1 Introduction

The 2021 $M_w7.2$ Haiti earthquake led to more than 2200 deaths and struck just over a decade after the devastating 2010 $M_w7.0$ earthquake which was one of the deadliest earthquakes recorded globally (National Geophysical Data Center, 1972). Both events occurred within a complex network of faults comprising the Enriquillo Plantain Garden Fault Zone (EPGFZ), which spans the Tiburon Peninsula in southern Haiti (Figure 1). Although the main Enriquillo Plantain Garden Fault (EPGF) has historically been mapped as a near-vertical fault which accommodates purely strike-slip motion (Calais et al., 2023; Manaker et al., 2008; Prentice et al., 2003; Mann et al., 1995), neither the 2010 nor the 2021 event had a pure strike-slip focal mechanism, nor did either clearly rupture this well-known fault as it is mapped. Instead, both recent ruptures initiated on a north-dipping fault segment which hosted significant dip-slip motion and then transferred westward to an adjacent steeply-dipping fault segment with primarily strike-slip motion (Calais et al., 2022; Okuwaki & Fan, 2022; Wen et al., 2023; Li & Wang, 2023; Yin et al., 2022). Both events also had major slip occurring off of the mapped EPGF: the 2010 event ruptured the blind Léogane thrust fault with seemingly no major slip accommodated on the

68

69

70

72

73

74

77

78

79

80

81

82

85

86

87

88

89

93

97

98

qq

101

102

103

104

105

106

108

109

110

111

112

113

114

116

117

118

119

EPGF, while the 2021 earthquake has been proposed to have initiated on a north-dipping thrust fault (it is unclear whether this is the EPGF or an unmapped fault) and then transferred westward to the mapped Ravine du Sud fault (Raimbault et al., 2023; Douilly et al., 2023) (Figure 1). Major questions remain about the fault geometry responsible for the 2021 event and how that geometry relates to the known fault system. It is also still not well understood why neither the 2010 nor 2021 event was a pure strike-slip event and, instead, each ruptured with two distinct patches of dip-slip and strike-slip motion on largely separate fault planes.

The combination of dip-slip and strike-slip motion observed in both 2010 and 2021 earthquakes is not unexpected given the tectonic setting of this fault zone. The EPGFZ occurs within the boundary between the North American (NA) and Caribbean (CAR) plates, which collide obliquely at an estimated rate of 18–20 mm/yr (DeMets et al., 2000). The Septentrional Fault, North Hispaniola fault, and the EPGFZ together accommodate both left-lateral and shortening motion, with the EPGFZ accommodating roughly half of the NA-CAR relative motion. A network of GNSS (Global Navigation Satellite System) stations throughout the region has allowed for the mapping of strain accumulation across the plate boundary (S. Symithe et al., 2015; Calais et al., 2023). Block modeling using GNSS data suggests two competing models for strain accumulation: the first model proposes that the EPGFZ accommodates about 6-7 mm/yr of left-lateral strike-slip motion, while the Jeremie-Malpasse (JM) reverse fault system off of the north shore of the Southern Peninsula (Figure 1) is responsible for accommodating 6-7 mm/yr of northsouth shortening (plate boundary-perpendicular motion). The second model proposes that the transpressive motion is accommodated primarily by the EPGFZ, with offshore thrust faults playing a less important role in shortening (Calais et al., 2023).

The 2010 earthquake rupture occurred to the east of the 2021 rupture (Figure 1) and both events increased Coulomb Failure Stress (CFS) on the section of the EPGF between the two ruptures (S. J. Symithe et al., 2013; Calais et al., 2022). This $\sim 40~km$ segment of the EPGF, however, has remained unruptured by either earthquake and it remains unclear why neither rupture breached this gap. Interestingly, centimeter-scale shallow creep was observed on sections of this unruptured segment following both the 2010 and 2021 events (Yin et al., 2022; Maurer et al., 2022; Raimbault, 2023).

Seismic and geodetic observations surrounding the 2021 earthquake provide critical insights into the dynamic rupture process. The event was recorded by the Ayïti-Seismes network, which, at the time of the earthquake, included four accelerometers (three of which were Raspberry Shake stations hosted by residents), and three broadband seismometers (Calais et al., 2022). Data from these stations were used to precisely locate a large cluster of aftershocks in the eastern portion of the rupture broadly delineating a north-dipping structure, with a more sparse cluster of aftershocks to the west (Figure 1a) indicating a near-vertical structure approximately coincident with the mapped RSF (Douilly et al., 2023). Interferometric Synthetic Aperture Radar (InSAR) geodetic imagery was captured from ALOS-2 and Sentinel-1 satellite missions, which resolved a detailed spatial pattern of co- and post-seismic ground deformation. InSAR observations constrained a region of uplift in the eastern part of the rupture consistent with thrust motion on a north-dipping structure. Left-lateral motion dominated to the west, where the InSAR captured offsets coincident with the Ravine du Sud fault reaching the surface (Yin et al., 2022; Raimbault et al., 2023; Li & Wang, 2023). GNSS offsets, which provide absolute static deformation measurements across the peninsula, confirmed the broad pattern of deformation observed in the InSAR data (Raimbault et al., 2023). Saint Fleur et al. (2024) conducted fieldwork following the 2021 event focused on documenting extensive surface cracking in response to the coseismic rupture. In the west, strike-slip cracks dominated, while the eastern section exhibited primarily thrust faulting. This variation aligns with the earthquake's mixed-mode rupture mechanism.

Several studies have investigated the slip distribution and fault geometry of the 2021 M_w 7.2 Haiti earthquake (i.e., Goldberg et al., 2022; Calais et al., 2022; Raimbault et al., 2023; Wen et al., 2023; Li & Wang, 2023; Okuwaki & Fan, 2022; Maurer et al., 2022). Despite differences in the inversion methods, considered observation datasets, and assumed fault geometries, most inversion studies agree that the earthquake ruptured at least two main fault segments: the rupture nucleated on an eastern north-dipping thrust segment where the slip reached ~ 2.5 -3 m without rupturing the surface. Then the rupture transferred westward to a sub-vertical strike-slip segment (broadly agreed to be the RSF) with ~ 1 -2 m of slip reaching the surface. Kinematic models consistently inferred source time functions (STFs) that contain at least two main peaks at 5-8 sec and 15-20 sec after the origin time, likely each coincident with a corresponding segment. STFs are in agreement with back-projection results which show two strong seismic radiation episodes aligned with kinematic model timing.

Despite the extensive work that has been done to understand the tectonics in Haiti through data collection networks (e.g. S. Symithe et al., 2015; Calais et al., 2022; Raimbault et al., 2023), geophysical surveys (e.g. Calais et al., 2023), and geologic mapping (e.g. Mercier de Lépinay et al., 2011; Saint Fleur et al., 2015, 2020, 2024; Prentice et al., 2003, 2010), gaps remain in our understanding of the complex faulting that drives seismic hazard, including the 2021 event.

Significant advances in the capabilities of dynamic rupture modeling techniques, enabled in part by the proliferation of high performance computing, provide an opportunity to understand the complex dynamics of the 2021 earthquake through 3D dynamic rupture simulation. Unlike kinematic or static slip inversions, which solve for slip distributions that sufficiently satisfy detailed observations, dynamic rupture models are forward simulations with a prescribed set of initial conditions and model parameters that allow the rupture to unfold spontaneously. Initial conditions consider fault geometry, material properties, fault strength (e.g., frictional properties, critical distance), and a description of pre-event stress on the fault. With these initial conditions it is possible to solve for the dynamic evolution of the rupture including fully dynamic wave propagation and permanent deformation (Ramos et al., 2022; Harris et al., 2011, 2018). While kinematic models can illuminate when and where slip occurred, dynamic rupture models can probe why the fault ruptured in a particular way, providing unique insights into the conditions that drove rupture. Dynamic rupture simulations have been used to study fundamental aspects of earthquake physics (e.g. Douilly et al., 2015; Gabriel et al., 2023), to assess earthquake hazards (e.g. Aochi & Ulrich, 2015; Douilly et al., 2017), to recreate notable rupture patterns in past earthquakes (e.g. Ma et al., 2008; Wollherr et al., 2019) and to discriminate between competing models of fault system geometries and faulting mechanisms (e.g. Palgunadi et al., 2020; Ulrich et al., 2019). In this study, we focus on identifying the conditions that control key observations of the 2021 M_w 7.2 Haiti earthquake. Using the dynamic rupture models, we simulate InSAR surface deformations, GNSS offsets, and source time functions to compare with observations. We aim to understand the drivers of key rupture characteristics that are inferred from the observations, primarily the spatial and temporal separation of left-lateral and reverse fault slip, and rupture transfer from the initial fault to the RSF to better understand the conditions that lead the observed rupture.

2 Methods and Model Setup

120

121

122

124

125

126

127

128

129

131

132

133

136

137

138

139

141

142

143

145

146

149

150

151

152

153

156

157

158

159

160

161

162

163

164

165

166

169

170

171

We solve the coupled dynamic rupture and seismic wave propagation problem using the open-source software SeisSol (https://github.com/SeisSol/). SeisSol is optimized for high performance computing, utilizing a Discontinuous Galerkin discretization with arbitrary high-order derivative (ADER) time integration and local time stepping on unstructured adaptive tetrahedral meshes (Dumbser & Käser, 2006; Heinecke et al., 2014; Uphoff et al., 2017; Krenz et al., 2021). SeisSol allows for the combination

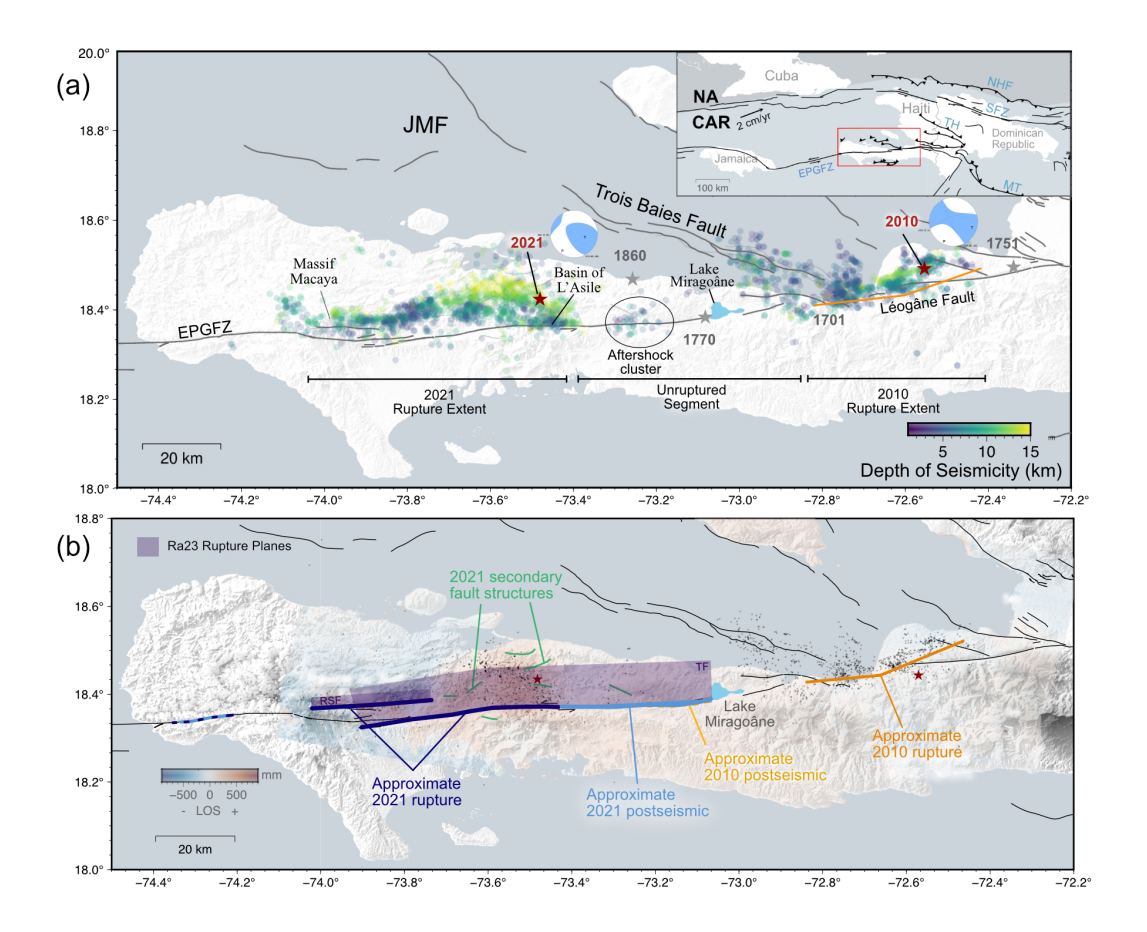


Figure 1. Overview of the tectonic setting of the 2021 earthquake. Top right inset shows the North American (NA) and Caribbean (CAR) tectonic plates with a relative plate motion of 2cm/yr and the major faults including the Enriquillo Plantain Garden Fault Zone (EPGFZ), the North Hispaniola Fault (NHF), Septentrional Fault Zone (SFZ), Trans-Hispaniola (TH), and Muertos Trough (TF) (a) Overview of the southern peninsula of Haiti, highlighting major geographic markers, 2010 and 2021 rupture extents and aftershocks, and historic earthquakes. Major historic earthquakes are marked by stars, with red stars highlighting the locations of the 2021 M_w 7.2 and 2010 M_w 7.0 epicenters; Aftershock locations are shown with circles, colored by event depths. Aftershock locations following the 2010 event are from Douilly et al. (2013), aftershock locations following the 2021 event are from Douilly et al. (2023). (b) Descending InSAR unwrapped interferogram is overlaid on topography, where red indicates the region of surface uplift over the eastern part of the rupture north of the fault. The two main fault planes used in this study, the Thrust Fault (TF), and the Ravine du Sud Fault (RSF) are shown with purple transparent rectangles (Ra23) adapted from Raimbault et al. (2023). The approximate extent of rupture constrained InSAR data (Yin et al., 2022)

of geometrically complex fault structures with region-specific fault and material properties. This is critical in Haiti where the geometric complexity of the fault zone has been interpreted to be central to the mechanics and strain partitioning of the EPGF fault system (Douilly et al., 2013; S. J. Symithe et al., 2013; Wang et al., 2018).

To construct a 3D dynamic rupture model, we must prescribe a set of parameters and initial conditions which govern the rupture including fault geometry, material properties, relative fault strength, and initial stress orientation and magnitude as summarized in Table 1 (Ramos et al., 2022). We choose parameters that reflect the best-available data and regional knowledge. In cases where relevant properties are unknown, we conduct sensitivity tests to determine the range of parameter values that allow for the matching of the earthquake observable. These parameters and initial conditions are described below.

2.1 Fault System Geometry

172

173

174

176

177

178

179

181

182

183

184

186

187

188

189

190

191

192

194

195

196

197

198

199

200

201

202

203

206

207

208

209

210

211

212

214

215

216

217

218

219

221

222

Fault geometry is a primary control on rupture evolution (Nielsen et al., 2000; Ando & Kaneko, 2018; Harris & Day, 1999). We develop a highly complex fault mesh to simulate the Haiti rupture, with 17 non-planar, 3D fault segments that curve and intersect over a 200+ km domain to accurately capture the fault complexity documented in the region. This geometry combines results from several sources including mapped faults and slip inversion studies (Figure 2). The geometry of the main two faults involved in the 2021 rupture is adapted from the Raimbault et al. (2023) study which distributes cosesismic slip from the 2021 event on two faults: (1) a thrust fault running subparallel to the EPGF (possibly the EPGF itself or a separate structure), herein called the Thrust Fault (TF) which dips north $66 \pm 4^{\circ}$; and (2) the Ravine du Sud Fault (RSF) which is a mapped near-vertical fault, dipping north $86 \pm 2^{\circ}$ (Figure 2). We extend the TF eastward from 73.2°W (where the Raimbault et al. (2023) geometry ends, Figure 1) to Lake Miragoâne, following the mapped EPGF trace to allow for the possibility that this is a continuous structure which extends beyond the observed rupture. Raimbault et al. (2023) developed this fault geometry based on a nonlinear kinematic finite fault slip inversion constrained by teleseismic data in Calais et al. (2022).

We include surrounding faults which were not observed to rupture coseismically to use as additional constraints on dynamic rupture simulations: the 2010 earthquake rupture geometry which is taken from Douilly et al. (2015); offshore thrust faults which produced significant aftershock activity following the 2010 earthquake are taken from analysis of seismic reflection surveys in Calais et al. (2023); centimeter-scale offsets across linear features located 10-20 km away from the main fault were observed to slip in the 2 weeks following the earthquake with InSAR imagery (Yin et al., 2022); and surrounding mapped vertical faults are taken from the comprehensive database in Saint Fleur et al. (2020). The purpose of including surrounding faults which were not observed as part of the main 2021 M_w 7.2 event is to act as constraints on the testable model space. For example, in some simulations we found that the offshore thrust faults included to the north of the EPGF failed spontaneously because they were well-aligned with regional stress field being tested (Figure S1). This allowed for the elimination of these regional stress configurations and to focus, instead, on testing other parts of the parameter space. The unstructured tetrahedral mesh includes topography (Farr et al., 2007) using the software PUMGen (https://github.com/SeisSol/PUMGen/). The mesh resolution is set to an element edge length of 200 m on the fault surfaces and gradually coarsens away from the faults to a maximum edge length of 15 km in the volume. The mesh includes a $300\times100\times40~\mathrm{km^3}$ high-resolution box within which frequencies of at least up to 1 Hz can be resolved. More information on the computational mesh is available in the supplemental information. The velocity model in the volume is adapted from Douilly et al. (2023) determined from aftershocks of the 2021 earthquake (Table S1). We force nucleation over a radius r_{crit} using friction reduction (see supplemental information).

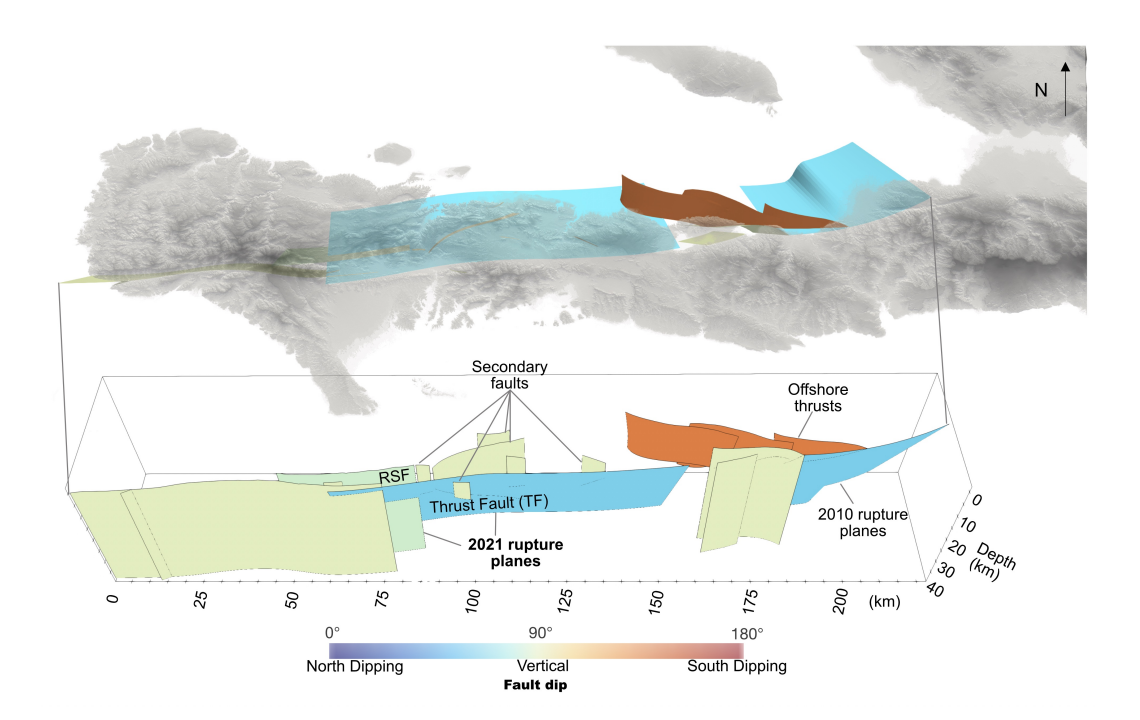


Figure 2. An oblique view of the fault geometry, with the top panel showing a top-down view of the topography of Haiti overlaid on the fault surfaces. The bottom panel shows a slightly adjusted view of the fault surfaces, labeled by source, including the Ravine du Sud Fault (RSF) and Thrust Fault (TF). Faults are colored by fault dip, with green indicating near-vertical faults, blue indicating north-dipping faults, and orange indicating south-dipping faults. 2021 M_w 7.2 coseismic rupture planes are taken from Raimbault et al. (2023), secondary faults observed from InSAR data are taken from Yin et al. (2022), offshore thrust faults are modified from Calais et al. (2023), the 2010 M_w 7.0 planes are adapted from Douilly et al. (2015), and surrounding mapped faults are taken from Saint Fleur et al. (2020).

2.2 Friction and Fault Strength

A linear slip-weakening (LSW) friction law is used to describe the frictional fault strength (Andrews, 1976; Ida, 1972). Coseismically, the slip-dependent fault weakening behavior governed by aging law rate-and-state friction is similar to that governed by linear slip-weakening friction (e.g. Bizzarri & Cocco, 2003; Garagash, 2021; Kaneko et al., 2008). Fault strength, τ , at any location on the fault is calculated using:

$$\tau = -C - min(0, \sigma_n)(\mu_s - \frac{\mu_s - \mu_d}{D_c}min(S, D_c))$$

Where C is the on-fault frictional cohesion, σ_n is the effective normal stress, μ_s and μ_d are the static and dynamic coefficients of friction, respectively, D_c is the critical slip distance, and S is the accumulated fault slip. SeisSol convention is that compressive stresses are negative so the $min(0, \sigma_n)$ term is always ≤ 0 . Faults begin to slip when local shear stress exceeds the local fault strength. Fault strength then decreases linearly from static to dynamic levels over the critical slip distance, D_c , where larger critical distance implies larger fracture energy. μ_s , μ_d , and D_c are defined throughout the fault geometry and are assumed to be spatially uniform, except in some notable circumstances where we vary the value of μ_s on some sections of the TF, as described in the results section. Following the procedure of Gabriel et al. (2023), we start by setting on-fault frictional cohesion to 0.5 MPa below 6 km on each fault and increase it linearly to 3 MPa at the surface to create a barrier to large surface ruptures.

2.3 Pre-stress Ratio

In a dynamic rupture simulation, only a small part of the fault needs to reach failure in order to initiate sustained rupture. The change in stress at the rupture front and dynamic stresses from seismic waves can raise the local shear stresses to exceed local fault strength, thereby sustaining the rupture. R, or the relative pre-stress ratio (Aochi, 2003; Ulrich et al., 2019), is the ratio of potential stress drop to full breakdown strength drop. R is related to the commonly used value S, which is a measure of fault strength relative to fault stress ($S = \frac{1}{R} - 1$, (Das & Aki, 1977)). The value of R resolved locally on a fault contains information both about that point's closeness to failure as well as its potential stress drop. The value of R is calculated from three components: 1) initial (static) fault strength, $\tau_y = \sigma_n \mu_s$; 2) final (dynamic) fault strength, $\tau_f = \sigma_n \mu_d$ and 3) initial shear stress, τ_0 , resolved on the fault surfaces (Figure 3).

The potential stress drop can be defined as the difference between initial shear stress and final shear stress ($\tau_0 - \tau_f$), while the potential strength drop is defined as the difference between the initial fault strength and the final shear stress. Under LSW, the final shear stress does not account for rapid co-seismic weakening and restrengthening (Madariaga, 1976; Gabriel et al., 2023) and so is equivalent to the dynamic shear strength. Accordingly, we can define:

$$R = \frac{\tau_0 - \tau_f}{\tau_y - \tau_f}$$

where τ_0 is the initial traction on the fault, τ_f is the final traction on the fault, τ_y is the fault strength which must be exceeded to initiate slip (Figure 3). We can then define R as:

 $R = \frac{\tau_0 - \mu_d \sigma_n}{(\mu_s - \mu_d)\sigma_n}$

where σ_n is the initial effective normal stress (Tinti et al., 2021). We note that because the effective normal stress will change throughout the rupture, the true stress drop and strength drop will not be exactly $\tau_0 - \tau_f$ nor $\tau_y - \tau_f$, respectively. Figure 3B shows a schematic profile of the fault stress and strength as a function of depth taken at one location on the fault. In the case of a fault near failure, the initial fault stress (black) will lie between the fault strength (green) and final stress levels (red). If rupture reaches this

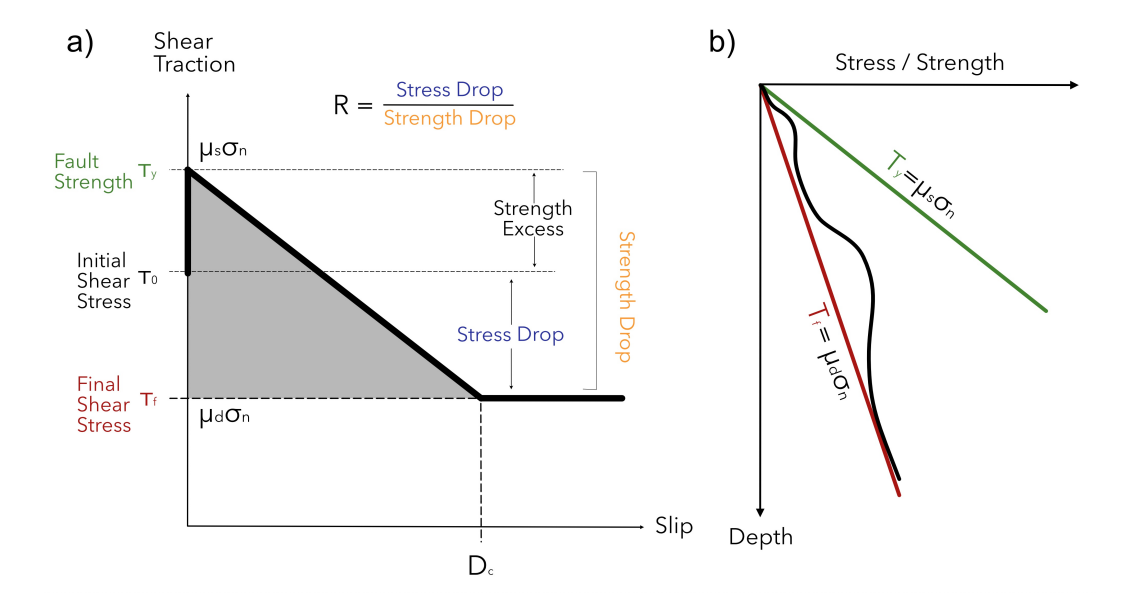


Figure 3. A schematic illustration of the relationship between shear traction, shear stress, and shear strength using Linear Slip Weakening law; a) Shear traction as a function of slip at a single point on the fault. τ_0 is initial stress, τ_y , is fault strength τ_f is the dynamic shear strength, i.e. the final shear stress of the fault. The strength excess is the difference between τ_y and τ_0 that must be overcome for the fault to fail and initiate slip. D_c is the critical distance over which the fault strength decreases linearly from its static level to its dynamic level; b) A schematic profile of shear stress and strength as a function of depth taken as a cross-section on some point on the fault at a single point in time. The black line shows a hypothetical profile of shear stress with depth, τ_y (green) shows a hypothetical profile of shear strength with depth, τ_f (red) shows a hypothetical profile of dynamic strength with depth. Figure adapted from Tinti et al. (2021).

location on the fault, shear stresses may be brought above the shear strength and then drop to the final shear stress. If at any point the stresses are insufficient to reach the static strength then rupture will not propagate.

The value of R can be resolved on any fault surface and depends on the initial stress, fault strength, and final stress on the given fault surface (Figure 4). We prescribe only the maximum prestress ratio R_0 , which is the prestress ratio of an optimally oriented fault in the stress field (Aochi, 2003) and effectively scales the overall magnitude of regional stresses. The local fault orientation relative to the stress controls the initial R value at any point on the fault with $R \leq R_0$. For $R = R_0$, the fault segment is optimally oriented with respect to the local stress conditions. For $R_0 = 1$ an optimally oriented fault segment is also critically stressed.

2.4 Initial Stress State

Following the work of Jia et al. (2023) and Hayek et al. (2024), we consider two main contributions to the stress distribution on the fault surfaces prior to the 2021 event: 1) regional stresses due to the accumulation of long-term regional tectonic loading; and 2) an a priori unknown distribution of on-fault stress variations on the fault surfaces which could be driven by the presence of subsurface asperities impacting the accumulation of stress on the fault or remaining stress heterogeneities left from past earthquakes (Figure 5). We develop dynamic rupture models which consider these sources of stress both

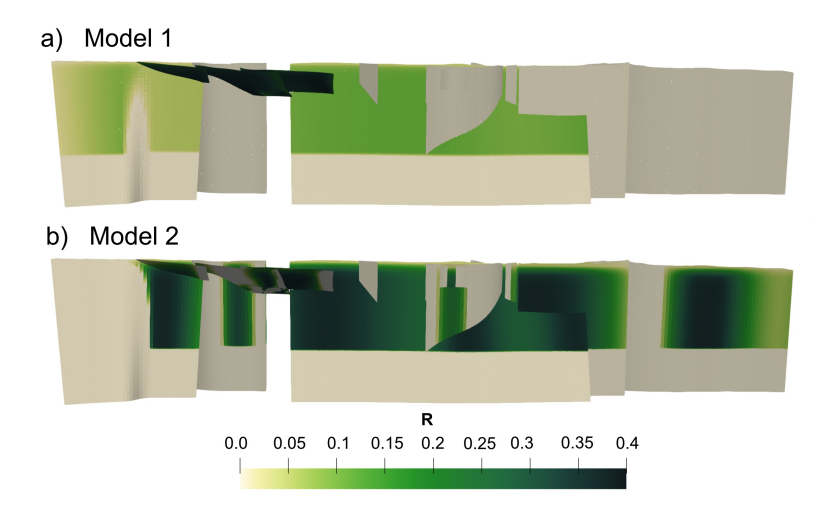


Figure 4. Pre-stress ratio values, R, resolved on the fault surfaces: a) R in the thrust faulting regime where the regional stress tensor has orientation $SH_{max} = 40^{\circ}$ and stress shape ratio, $\nu=0.5$; b) R in the strike-slip faulting regime where the regional stress tensor has orientation $SH_{max} = 50^{\circ}$ and stress shape ratio, $\nu=0.0$;

separately and in combination to better understand their unique contributions to the observed rupture. We expect the regional stress field to broadly encourage left-lateral strikeslip and thrust motion on the main two faults, while the heterogeneous stress field may provide a more nuanced spatial pattern of stress concentrations. We note that this setup does not explicitly account for any stresses imparted by the 2010 earthquake. Here we describe the theory and methods used for each of these stress sources.

2.4.1 Regional Stress Field

We calculate a tectonically-driven regional stress state across the Peninsula (Figure 5a), assuming Andersonian stress conditions, where one principal stress component is assumed to be vertical (Heidbach et al., 2018; Simpson, 1997). We calculate the stress tensor at every point on the faults, comprising what we call the "regional-only" stress field. The orientation of the principal stresses σ_1 , σ_2 , and σ_3 (where $\sigma_1 > \sigma_2 > \sigma_3$) depend on the assumed faulting regime and the azimuth of the maximum horizontal compressive stress SH_{max} (measured clockwise from north) while their amplitude depend on the stress shape ratio ν , the relative prestress level R_0 of an idealized fault optimally oriented for failure (see section 2.3), and the effective lithostatic stress σ'_{zz} (Ulrich et al., 2019).

The faulting regime depends on which component corresponds to the maximum horizontal principal stress SH_{max} , the minimum horizontal principal stress, SH_{min} , and the vertical principal stress component, S_v . In the thrust faulting regime, $SH_{max} > SH_{min} > S_v$, whereas in the strike-slip faulting regime, $SH_{max} > S_v > SH_{min}$ (Heidbach et al., 2018) (Figure 6). The stress shape ratio, ν , scales the relative amplitudes of principal stresses and is defined as:

$$\nu = \frac{s_2 - s_3}{s_1 - s_3}$$

where s_1 , s_2 , and s_3 , are the principal stress components ordered from largest to smallest. The faulting regime impacts the meaning of ν . For example, in a strike-slip faulting regime, ν =0.5 indicates pure strike-slip, ν < 0.5 indicates transpression, while ν > 0.5 indicates transtension.

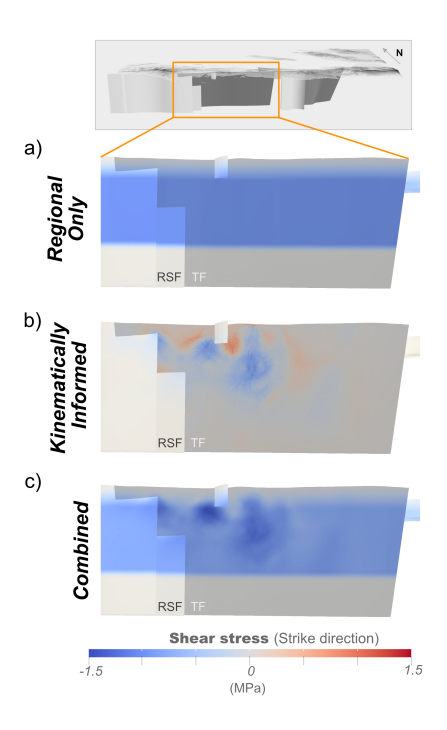


Figure 5. Initial shear stresses resolved on the fault surfaces, where negative shear stresses in the strike direction encourage left-lateral slip. : a) tectonically-driven regional stresses, where deviatoric stresses are tapered to zero below the seismogenic depth starting at 25 km depth; b) stresses derived from the Kinematically Informed Heterogeneous Stress method; c) the combined regional and Kinematically Informed Heterogeneous Stresses.

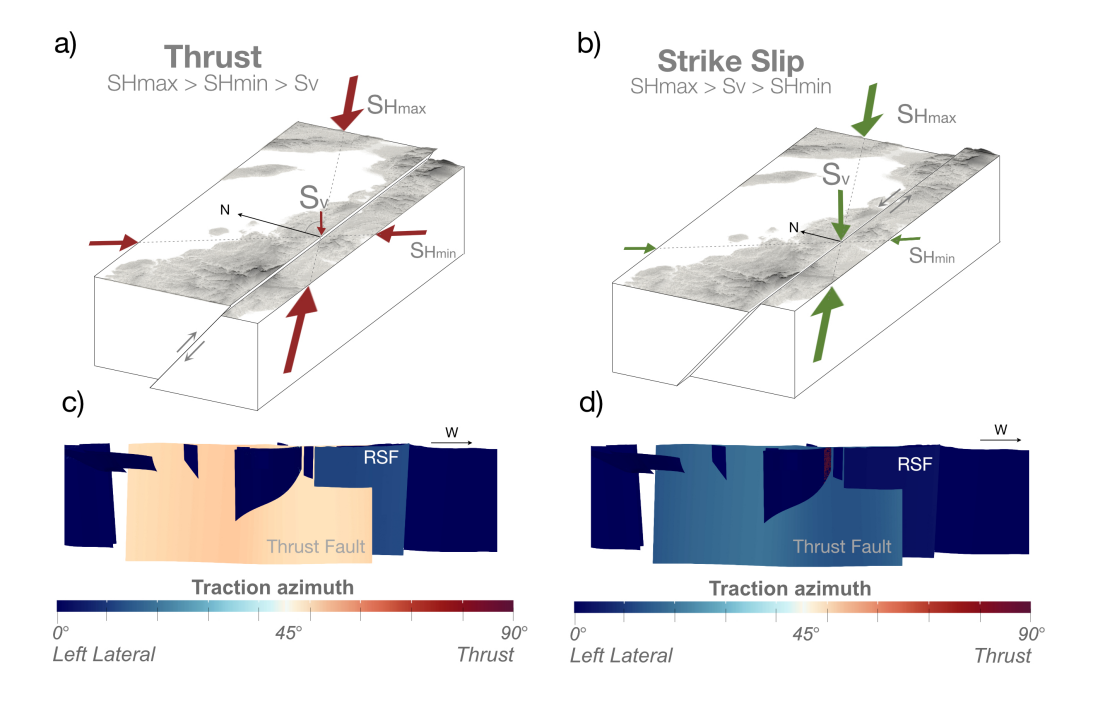


Figure 6. Schematic representation of regional stress tensors acting on a simple block model. The relative size of the principal stress components are shown schematically with arrows. The topography of Haiti is shown on the top face and a simple north-dipping fault is depicted, schematically representing the TF: a) Schematic of a thrust faulting regime where the minimum horizontal component SH_{min} is larger than the vertical component, S_v ; b) schematic of a strike slip faulting regime where the minimum horizontal component SH_{min} is smaller than the vertical component, S_v ; c) corresponding shear stress direction in the thrust faulting regime with $\nu = 0.5$ resolved on the fault surfaces. This results in a higher angle of the traction vector (more thrust motion) on the north-dipping TF; d) corresponding shear stress direction in the strike slip regime with $\nu = 0.0$ resolved on the fault surfaces. This results in a shallower traction vector (mores strike-slip motion). Adapted from Heidbach et al. (2018)

314

315

316

318

319

320

321

322

323

325

326

327

328

330

331

332

333

334

335

338

339

340

341

342

343

344

345

346

347

348

349

350

351

352

353

356

357

358

359

360

361

We compare different effective lithostatic stress σ'_{zz} assumptions with depth (Madden et al., 2022). First, we consider assuming that the fluid pressure Pf throughout the crust is proportional to the lithostatic stress σ_{zz} : $Pf = \gamma \sigma_{zz}$, where $\sigma_{zz} = \rho gz$ and $\gamma =$ ρ_{water}/ρ , the fluid-pressure ratio. The effective lithostatic stress is thus $\sigma'_{zz}=(1-\gamma)\sigma_{zz}$ (Aochi & Ulrich, 2015; Ando & Kaneko, 2018). Alternatively, we consider a fluid overpressure assumption (Rice, 1992; Madden et al., 2022; Suppe, 2014) in which, at depth, the pore fluid pressure gradient mirrors the lithostatic stress gradient, leading to constant effective lithostatic stress at depth. This behavior was observed in accretionary prisms in subduction zones (Suppe, 2014), which is an environment comprising the Haitian southern peninsula. In our implementation of this assumption, we use a pore fluid pressure ratio $\gamma = 0.34$ and taper stresses to 52 MPa at 6 km depth (Gabriel et al., 2023). The lithostatic stress assumption leads to stresses continuously increasing with depth and has commonly been used to model other earthquakes (Aochi & Ulrich, 2015). However, for this event, seismicity extends to nearly 30 km depth, resulting in large stresses on the fault below the hypocenter which prevented sustained rupture. When rupture did occur, stress drops tended to be extremely large, producing large slip magnitudes (>10 m in some cases), supershear rupture and other unobserved effects, even when minimizing strength drop $(\mu_s - \mu_d)$ and regional stress scaling (R_0) . When using the fluid over-pressure condition, we observed more realistic stress drops, slip magnitudes, and rupture velocities. We therefore use the fluid over-pressure assumption in all the following simulations.

We use a stress modulation function, $\Omega(z)$ (Ulrich et al., 2019), to smoothly taper deviatoric stresses to zero at seismogenic depths between 25-28 km, to mimic the brittle ductile transition at the bottom of the seismogenic zone. This depth range is chosen based on the distribution of relocated aftershock seismicity which extends to ~ 30 km depth (Douilly et al., 2013, 2023). Kinematic slip inversions also found the slip distribution to be largely limited to above 20 km (Goldberg et al., 2022; Calais et al., 2022).

2.4.2 Stress heterogeneity on the fault surface

Variations in pre-event stress on a fault plane may result from past ruptures on that fault or nearby faults, unmodeled geometric complexity of the faults, local variations in fault strength, fluid pressure, or unknown local variations in tectonic loading. These sources of stress are not taken into account when only a uniform regional loading is considered. The distribution of stress drop resulting from an earthquake can reflect such pre-event stress heterogeneities and can therefore be used to help constrain the initial stress distribution of a dynamic rupture model (Miyatake, 1992).

We use a Kinematically Informed Heterogeneous Stress technique in which a slip model is used to calculate the change in stresses on the fault surfaces due to coseismic slip. The Raimbault et al. (2023) GNSS and InSAR-derived static slip distribution is assumed as the final distribution of slip on the TF and RSF fault surfaces and imposed as a boundary condition in a pseudo-static simulation (Tinti et al., 2005; Yang et al., 2019) (see section 3 of the supplementary document for more details about this technique). The resulting static stress change is shown in Figure 5b. These Kinematically Informed Heterogeneous Stresses can be multiplied by a scaling factor, α (typically $0 < \alpha < 1$, scaled through trial and error), and added to the regional stress tensor components to describe more realistic initial stress distribution on the fault. This approach has been used to dynamically model a variety of events (e.g. Tinti et al., 2021; Jia et al., 2023; Wang et al., 2018; Hayek et al., 2024; Glehman et al., 2024) and can be particularly useful in regions like Haiti where no other detailed constraints are available. This approach has the advantage of using the same computational mesh and fault geometry as is used in the subsequent dynamic rupture simulations. A more detailed description of the implementation of this technique can be found in the Supplemental Materials (Section S3).

3 Constraining the regional stress state

We seek to orient and scale the regional stress tensor to approximate the broad transpressional tectonic loading of the TF and RSF. The faulting regime in combination with the orientation of the principal horizontal stress component (SH_{max} orientation) and scaling of the principal stress components relative to one another (stress shape ratio, ν) determines the direction of traction (i.e. the direction of shear stress) resolved on the fault surfaces. Past modeling studies in this region have assumed a strike-slip faulting regime (Douilly et al., 2015). The SH_{max} orientation for the 2010 earthquake has been estimated using GNSS block modeling and dynamic rupture modeling to be approximately $40-50^{\circ}$ clockwise from North (S. Symithe et al., 2015; Calais et al., 2015, 2023). However, these assumptions have not been tested for consistency with the 2021 earthquake rupture. Additionally, stress orientations are associated with large uncertainties, at best \pm 15° at the surface and \pm 25° at depth (Heidbach et al., 2018) and there may be significant variation across the peninsula (Calais et al., 2015).

Therefore, before developing any dynamic simulations, we first conduct a parameter exploration aimed at constraining the orientation and shape of the regional stress field in the vicinity of the 2021 rupture. To do this, we examine the impact of SH_{max} orientation and ν on the direction of traction resolved on the TF and RSF faults. If we assume that the direction of initial shear traction on a fault is parallel to the direction of slip (rake) during rupture, then we aim to find the range of regional stress conditions that produce traction aligned with rake observed during the 2021 earthquake. The rake and direction of traction are both defined according to Aki and Richards conventions (Aki & Richards, 1980) where 0° is pure left-lateral motion and 90° is pure thrust motion (Figure 7). Slip distributions from inversion studies report the rake of the first sub-event to be greater than 40° (a combination of thrust and left lateral motion), while the rake of the second sub-event on the RSF is less than 30° (closer to pure left-lateral motion) (Li & Wang, 2023; Calais et al., 2022; Raimbault et al., 2023), consistent with InSAR observations.

We resolve the average traction direction on the TF and RSF for a range of SH_{max} orientations from $30-70^{\circ}$ and ν values from 0.0 to 0.7, for both the case where $S_v >$ SH_{min} (thrust faulting regime) and the case where $SH_{min} > S_v$ (strike slip faulting regime). Figure 7 shows the impact of SH_{max} orientation and ν on the direction of the average traction on the RSF and TF in the thrust faulting regime. In the thrust faulting regime, increases in the stress shape ratio, ν , result in a traction vector with a larger dip slip component, while clockwise rotation of the orientation SH_{max} reduces the dip slip component of the traction vector. Changing the orientation of the stress tensor, SH_{max} , also changes the direction of traction across the faults depending on the change in strike along the fault, but the effects are small ($\pm 5^{\circ}$, Figure 7, Figure S2). Traction direction on the RSF is less sensitive to parameter changes and remains less than 30° in most parameter combinations (Figure 7). We find that in the strike slip faulting regime, the traction vectors generally have an insufficient components of dip slip to match observations. Even when $\nu = 0$ (the transition point between strike slip and thrust faulting regimes where $Sh_{min} = S_v$), the rake on the TF is only 15-20° (Figure S5). This case is explored more fully in the first dynamic rupture simulation (Model 2).

In addition to the alignment of the traction direction to the expected rake, we also consider how the choice of SH_{max} orientation and ν impacts the pre-rupture stress magnitude and strength of the fault. If, for example, stresses on the fault are not large enough to overcome the fault strength, then rupture cannot be sustained. We calculate the prestress ratio, R, across the fault surfaces, where higher R indicates that the fault is more likely to sustain rupture. We find that as the traction azimuth increases (closer to pure thrust motion), R tends to decrease (Figure S5). R values are highest for low values of ν in the thrust-faulting regime.

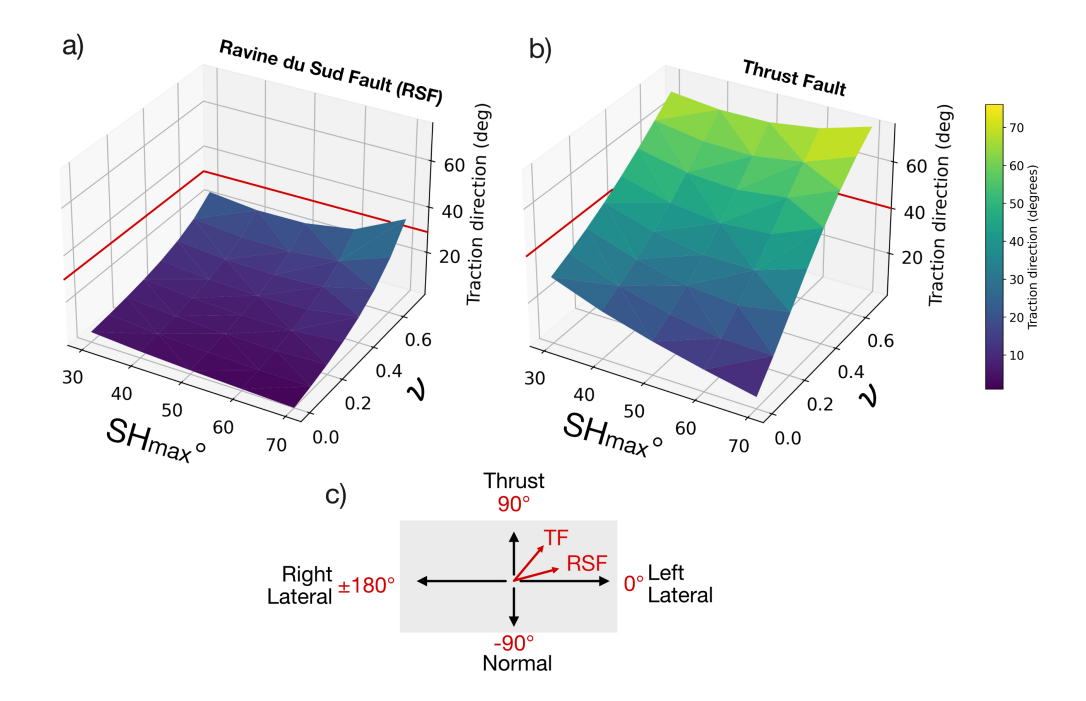


Figure 7. Plot showing the impact of SH_{max} and ν on the direction of the average traction vector on both the RSF and TF in the thrust faulting regime; a) on the RSF, the expected traction direction is less than 30° (shown with the red line); b) on the TF, the expected traction direction is greater than 40° (red line); c) schematic of Aki and Richards rake and traction direction convention.

We identify a range of values of ν and SH_{max} that balance agreement between the direction of traction within 15 degrees of the slip model rake while maintaining a high R value: we expect values of ν to fall between 0.2 and 0.5 and orientations of SH_{max} between 40-60° in the thrust faulting regime. In full dynamic simulations using these ranges, the modeled surface deformation produces the expected the ratio of strike slip to dip slip motion implied by the InSAR data and GNSS observations, confirming this range of regional stress parameters.

4 Dynamic Rupture Modeling

4.1 Modeling Approach

Having identified a range of plausible regional stress parameters (SH_{max} orientation and ν), we now begin designing and running dynamic rupture simulations with the goal of better understanding the conditions which led to the observed 2021 rupture. Our approach for each suite of simulations is to begin with some assumptions about the initial conditions, then run and refine simulations, eventually producing a rupture most consistent with observations given the initial assumptions. By comparing the simulation outputs to key rupture observations, we learn more about rupture dynamics and can then update our assumptions about the initial conditions before running a new suite of simulations. In general, we aim to begin with the simplest assumptions and add complexity to the initial conditions only as needed.

Table 1. Table of parameters and definitions used in the dynamic rupture modeling setup.

Symbol	Parameter
$\overline{D_c}$	Critical Linear Slip Weakening dis-
	tance
μ_s	Static coefficient of friction
μ_d	Dynamic coefficient of friction
r_{crit}	Nucleation radius
α	Weight of Kinematically Informed
	Heterogeneous Stresses
R_0	Scaling of prestress ratio, R , for an
	optimally oriented virtual fault. Ef-
	fectively scales regional stress magni-
	tudes.
SH_{max}	Orientation of maximum principal
near	stress component for regional stress
	tensor.
ν	Stress Shape Ratio
C_0	Frictional Cohesion

Table 2. Parameter values for the five dynamic rupture models discussed

Parameter	Model 1	Model 2	Model 3	Model 4	Model 5
$\overline{D_c}$	0.03 m	0.05 m	0.06 m	0.06 m	0.02 m
μ_s	0.5	0.57	0.5	0.52	0.52
μ_d	0.15	0.5	0.16	0.16	0.16
r_{crit}	$7~\mathrm{km}$	$7~\mathrm{km}$	$7~\mathrm{km}$	$7~\mathrm{km}$	$7~\mathrm{km}$
SH_{max}	40°	50°	40°	40°	$40 50^{\circ}$
ν	0.5	0.0	0.5	0.5	0.0 - 0.5
R_0	0.4	0.4	0.4	0.4	0.14 - 0.41
α	0.0	0.0	0.9	0.9	0.7
C_0	3 MPa	3 MPa	3 MPa	3 MPa	2 - 5 MPa

In the development of the 5 presented models, summarized in Table 2, we conducted several hundred full dynamic simulations, varying parameters over a range of reasonable values. Because a systematic variation of all parameters in concert with each other is difficult to achieve, we prioritize incorporating realistic levels of static and dynamic frictional resistance and stress drop. An order-of-magnitude stress drop can be estimated by $R_0(1-\gamma)\sigma_c(\mu_s-\mu_d)$ (Ulrich et al., 2019) so a variety of combinations of these variables could result in the same stress drop estimate. Therefore the results that we present could feasibly be represented with different parameter combinations. Over all simulations, the parameter ranges include frictional strength of $0.2 < \mu_s < 1.0$, $0.1 < \mu_d < 0.5$, both lithostatic and fluid overpressure assumptions, regional stress magnitudes $0.1 < R_0 < 0.6$, stress shapes $0.0 < \nu < 0.5$, and principal stress orientations $40^{\circ} < SH_{max} < 60^{\circ}$.

For each simulation, we compare to six key observations and characteristics of the earthquake:

- 1. separation of strike slip and dip slip motion;
- 2. unilateral westward rupture;

435

436

437

438

439

442

443

444

445

446

447

449

450

- 3. rupture transfer from the TF to the RSF;
- 4. total moment magnitude $(M_w7.2)$;

5. source time function (detailed below);

452

453

454

455

456

457

458

459

462

463

468

469

472

473

474

477

478

479

480

481

485

486

488

491

492

493

498

499

6. surface deformation observations (InSAR and GNSS, detailed below).

We compare the simulated source time functions to those from Goldberg et al. (2022); Okuwaki and Fan (2022); Calais et al. (2022). Three InSAR interferogram pairs are used for comparison to model results. JAXA ALOS-2 interferograms are used because the L-band wavelength of this mission better captures large surface deformations in this highly vegetated region, especially in the near-fault region (Yin et al., 2022). Two ascending (A043 and A042) and one descending (D138) path interferograms covering the coseismic period are used from Yin et al. (2022). GNSS static offset data is taken from campaign data published in Raimbault et al. (2023).

In the following sections we present the results of five dynamic rupture simulations which each represent a major evolution in the initial condition assumptions. We address how each informed our understanding of the rupture dynamics of the 2021 earthquake and the conditions which may have led to it.

4.2 Model 1: Regional stress in the thrust regime

We begin with a simple dynamic rupture model where pre-rupture stress conditions across the fault system are defined by a single regional stress orientation and shape. We seek to determine if a single regional stress field, when applied to the assumed complex fault geometry, is sufficient to create dynamic rupture both on the TF and RSF with separated strike slip and dip slip motion. If sufficient, this would imply that the earthquake is primarily a result of the broad regional transpressive stress field in the presence of existing faults.

Based on the results from the sensitivity study in Section 3, this initial model imposes a regional stress tensor oriented at $SH_{max} = 40^{\circ}$ and with stress shape ratio, $\nu =$ 0.5 in the thrust-faulting regime. We expect these conditions to create shear traction and therefore slip on the TF with an average rake of $\sim 51^{\circ}$ and slip on the RSF with an average rake of $\sim 12^{\circ}$ (Figure 7), consistent with the expected rake from slip inversions. We vary the values of the remaining parameters to find a combination which sustains dynamic rupture beyond the forced nucleation zone but does not produce an unreasonably large earthquake (i.e. $M_w \leq 7.4$). For this model, the parameters we find are $D_c =$ $0.03 \text{ m}, \mu_s = 0.5, \mu_d = 0.15, R_0 = 0.4, \text{ and } C_0 = 3MPa \text{ at the surface. This results}$ in a M_w 7.39 earthquake, which produces slip on nearly the entire TF with an average rupture velocity of ~ 3.5 km/s (Figure 8a). There is a maximum of ~ 2.5 m of slip developing on the fault, which is comparable to estimates of peak slip from slip inversions. However, slip occurs over the entire extent of the TF, resulting in surface deformation that far exceeds that observed by InSAR and GNSS (Figure 8c), and produces significant mismatch with the expected source time function (Figure 8b). Importantly, this scenario fails to recreate dynamic rupture transfer to the RSF, one of the key characteristics of this earthquake. We therefore conclude that a simple regional stress field does not result in the observed coseismic faulting pattern when all properties of the fault are assumed constant along-strike.

4.3 Model 2: Regional stress in the strike slip regime

In order to test which conditions are controlling the transfer of rupture from the TF to the RSF, we again impose a single regional stress tensor, but this time in the strike-slip faulting regime. We select the orientation $SH_{max}=50^{\circ}$ and stress shape ratio, $\nu=0.0$ (i.e. where $S_2=S_3$), even though, based on the results in Section 3 (Figure 7), we expect that this combination will result in slip on the TF with rake too shallow (i.e. not enough thrust motion) to match surface deformation observations. We again vary the values of the remaining parameters to find a combination which sustains rupture be-

yond the forced nucleation zone but does not produce an unreasonably large rupture ($M_w \le 7.4$). We find that the following values achieve this balance: $D_c = 0.05$ m, $\mu_s = 0.57$, $\mu_d = 0.5$, $R_0 = 0.4$, and $C_0 = 3MPa$ at the surface. Note the need to prescribe a relatively dynamically strong fault with a low strength drop ($\mu_s = 0.57$ and $\mu_d = 0.5$) in order to recreate the observed magnitude of slip. If the dynamic coefficient is decreased to make the fault dynamically weaker, then the peak slip on the fault increases to produce unreasonably large earthquakes.

After nucleation, the rupture propagates bilaterally on the north-dipping TF. After approximately 17 seconds of rupture time, nearly the entire TF has slipped on the order of 1 m. The rupture front to the west reaches the termination of the TF, \sim 15 km west of the intersection with the more steeply dipping RSF. Despite the geometric barrier formed by this intersection at about \sim 14 km depth, dynamic rupture successfully transfers to the RSF almost immediately. The final moment magnitude of the earthquake is M_w 7.23, close to the observed moment magnitude of M_w 7.2. However, the maximum slip of \sim 1.4 m is smaller than the expected \sim 2.3 m and remains relatively constant across the TF and RSF.

In this model, like Model 1, slip on the TF extends over the entire fault as opposed to the expected compact rupture centered around 73.6°W (Figure 9a). This results in a broad first moment rate peak inconsistent with STF estimates (Figure 9b) and does not generate inferred troughs and multiple peaks in the source time functions. Two to three pulses of slip are inferred in many past studies of the 2021 earthquake, including back-projection results (Okuwaki & Fan, 2022) and joint teleseismic inversion studies (Goldberg et al., 2022), which indicates that there is at least one delay in moment release which is important to recreate (Figure 9b).

Slip on the TF has a rake of $\sim 16\text{-}18^\circ$ and slip on the RSF has a rake of $\sim 2\text{-}3^\circ$, closer to pure strike slip motion (Figure S6). While this change in rake between the TF and RSF produces some of the expected separation of strike slip and dip slip motion, it fails to produce sufficient thrust motion on the TF to match observations, estimated from slip inversions to be $40+^\circ$. The descending LOS image shows this mismatch (Figure 9c), where the observed LOS shows a lobe of positive deformation (consistent with uplift) north of the TF surface trace, whereas the simulated LOS deformation remains negative north of the TF surface trace (Figure 9c, RMS = 0.122). This comparison illustrates that the vertical motion produced by the TF in this simulation must be larger relative to the left lateral motion in the LOS direction to agree with InSAR observations.

Producing dynamic rupture transfer coupled with sufficient thrust motion on the TF is difficult with a single regional stress field because the regional stresses required to produce enough thrust motion on the TF to match the observations, tend to result in very low pre-stress levels on the RSF (i.e. low R). This is shown in Figure 4, which compares the initial values of R resolved on the fault surfaces for Model 1 and Model 2. Model 1, which produces the correct rake on the TF has near-zero R values on the RSF, which explains why it does not rupture easily. Model 2, which produced rupture transfer but insufficient dip slip motion on the TF with high R values on both TF and RSF (reaching up to R=0.37 for Model 2, versus maximum R=0.14 for Model 1, Figure 4).

Models 1 and 2 together support the interpretation that there is a tradeoff between producing the expected rake on each fault plane and the likelihood of rupture transfer between faults. A regional stress field closer to the thrust regime promotes shear stresses with different traction directions on the RSF and TF, but comes at the cost of discouraging rupture transfer. Whereas, a regional stress tensor closer to a pure strike slip regime promotes rupture transfer but the difference in rake between the two faults shrinks, leading to a mismatch with observed InSAR surface deformations. Regional stress fields between these two end member cases $(0.0 < nu < 0.5, 40^{\circ} < SH_{max} < 60^{\circ})$ were explored to test if any of the intermediate cases could produce both the decomposition of motion

into strike-slip on the RSF and ip-slip on the TF and rupture transfer between faults, but none could accomplish both simultaneously. An example of such a simulation is included in the supplementary materials (Figure S2). We therefore conclude that no single regional stress tensor alone can explain both the direction of slip consistent with In-SAR data and the spontaneous rupture transfer between fault segments. Some along-fault variation in the initial stress shape and orientation of the regional stress tensor may be contributing to rupture transfer and the compact nature of the resulting slip patches.

553

554

558

559

560

563

564

565

567

568

571

572

573

575

576

577

578

579

580

583

584

585

586

587

591

592

593

596

597

598

600

601

4.4 Model 3: Combined Regional and Kinematically Informed Heterogeneous Stresses in the Thrust Regime:

It is impossible to know the true initial stress state on the fault surfaces prior to the earthquake. However, we can carry out an experiment to see how initial stress heterogeneity may influence the dynamic rupture. In Model 3, we introduce stress heterogeneity on the faults determined from a static slip model (Raimbault et al., 2023) using a Kinematically Informed Heterogeneous Stress simulation (Sec.2.4.2). The introduction of these stresses adds variation to the background regional stress resolved on the fault surfaces (see Methods section), representing smaller-scale stress variation that is not captured by the broad regional tectonic loading alone. We expect that slip will concentrate more compactly on parts of the fault with higher initial stress. For this simulation, we chose a regional stress field oriented with $SH_{max}=40^{\circ}$ and $\nu=0.5$ in the thrust faulting regime. We weight the Kinematically Informed Heterogeneous stresses using $\alpha=0.9$. Given these conditions, the combination of parameters which sustains rupture but produces a $M_w \leq 7.4$ event is: $D_c=0.06$, $\mu_s=0.5$, $\mu_d=0.16$, $R_0=0.4$, and $C_0=3MPa$ at the surface.

After nucleation, the TF ruptures away from the hypocenter bilaterally. Within 20 seconds, the western rupture front has reached the intersection with the RSF but fails to transfer. By 30 seconds it has ruptured the entire extent of the TF and rupture still does not transfer to the RSF. However, unlike previous ruptures, in this simulation slip concentrates in patches near the center of the TF ($\sim 73.6^{\circ}$ W), with a peak slip of ~ 2.4 m which decreases away from the center of the fault (Figure 10a) and the final moment magnitude is M_w 7.31. This results in better agreement with the InSAR data, where deformation is concentrated over the observed coseismic region (Figure 10c). However, the entire TF still ruptures, creating disagreement with the extent of deformation in the In-SAR observations (where the simulation creates surface deformation which extends further to the east and west compared to the observations) and the width of the single moment rate peak (which is much wider when compared to the observations, shown in Figure 10b). The combination of rupture transfer from the TF to the RSF with 40+° rake on the TF remains elusive. Model 3 shows that while initial stress heterogeneity can act to concentrate slip spatially on the fault, it does not appear to control the large-scale features of rupture, including the rupture extent, overall energy release of the event, or dynamic rupture transfer from the TF to the RSF (see Supplement). Further discussion of the requirement for stress heterogeneity is included in Section 5.

4.5 Model 4: Introducing fault strength variations

When constructing the fault geometry, we purposely extended the TF fault past the limits of the observed rupture in order to understand what factors influence the extent and location of rupture (Figure 2). In all experiments to this point, slip on the TF extended to the limits of the fault specified in the geometry, well beyond the actual rupture. It was also difficult to recreate the timing of the rupture transfer from the TF to the RSF. In this model, we introduce heterogeneities in the along-fault frictional properties on the TF to investigate whether a change in fault properties that limits slip to the east and west could be influencing rupture transfer to the RSF and the extent of slip. We note that, due to dynamic-trade-offs, choosing an increased μ_s can be viewed as a

proxy for locally lower initial shear stresses, e.g., reflecting stress shadows of previous regional earthquakes (e.g. Taufiqurrahman et al., 2023), or unmodeled changes in fault geometry. What we represent in this model as changes in fault strength could alternatively represent termination of the TF or changes to the strike or dip of the TF structure at these locations.

604

605

608

609

610

613

614

615

617

618

619

620

621

622

625

626

627

629

630

631

632

633

634

635

637

638

639

640

641

642

645

646

647

648

650

651

652

653

The InSAR data (the main observation indicating the rupture extent) shows minimal surface deformation close to the mapped EPGF approximately east of 73.4°W (point Y in Figure 11b) and west of 73.8°W (point X in Figure 11b; Figure 12c). In Model 4, we increase the static coefficient of friction (μ_s) to 1.0 east and west of these locations to discourage rupture propagation. We otherwise leave $\mu_s = 0.52$ as in previous simulations. The extent of these static strength changes are shown in Figure 12d. All other parameters are identical to the previous simulation (Model 3).

After nucleation, the dynamic rupture propagates on the TF, however, instead of rupturing bilaterally as in previous simulations, the rupture front quickly encounters the increased static strength of the fault to the east (east of point Y on Figure 11b), limiting slip extent. To the west, after about 15 seconds, the rupture front encounters increased static strength west of point X (Figure 11b), limiting the rupture. Despite the rupture propagating past the beginning of the intersection with the RSF, it does not transfer to the RSF fault. The limitation of the spatial extent of the slip on the TF creates a compact rupture that produces the expected surface deformation pattern in the eastern part of the rupture (Figure 12c). These increases in fault strength also result in a narrower moment rate pulse which more closely resembles the first peak of the Goldberg et al. (2022) source time function (Figure 12b). The maximum slip is ~ 2.3 m, similar to the Raimbault et al. (2023) slip distribution, and the limited lateral extent of slip means that the moment magnitude of the rupture is smaller, $M_w 7.10$. This is less than the observed $M_w 7.2$ rupture but that is expected given the non-rupture of the RSF.

We find that the lack of rupture propagation from the TF to the RSF is a persistent feature of all ruptures which assume a thrust faulting regime with a high stress shape ratio ($\nu = 0.3$ - 0.5, not all simulations shown). This remains true even when the strength of the RSF is reduced, and when the pre-stress levels on the RSF are increased (achieved by increasing R_0). The lack of RSF rupture in Model 4 is evident in the mismatch between the simulated and observed InSAR data (Figure 12c). The simulated InSAR data produces no surface rupture on the RSF as opposed to what is observed in track A043 (RMS=0.276). We also note the lack of multiple moment rate peaks in the source time function (Figure 12b) and that there is a mismatch at the two GNSS sites, CAMR and CAMY, just south of the RSF (Fig13a). GNSS vectors very close to a fault are often difficult to match exactly, for example due to fault fling (e.g. Calais et al., 2010). The fit to stations CAMR and CAMY might be improved by further refining the details of the western termination of the RSF. Despite the non-rupture of the RSF, the lobe of uplift which is readily apparent in the Descending InSAR Scene is generated by the increased shear strength of the eastern portion of the TF (RMS=0.079). The simulated GNSS data surrounding the rupture on the TF demonstrates a close match to the observed data (Figure 12a). Model 4 demonstrates that changes in friction along the TF is one way to implement along-strike variations in fault properties and effectively limits the rupture extent.

4.6 Model 5: Combined Regional and Kinematically Informed Heterogeneous Stresses with Lateral Variation in Regional Stress Field

In all previous simulations in the thrust faulting regime, dynamic rupture did not transfer to the RSF. The following experiment tests the hypothesis that an along-strike change in the regional stress field would favor rupture transfer while preserving the large amount of dip-slip motion on the TF. We combine the stress conditions that produced rupture transfer from the TF to the RSF in Model 2 and the conditions which produced sufficient thrust motion on the TF in Model 4. To do this, we set $SH_{max}=50^{\circ}$, $\nu=0.0$ on the RSF and $SH_{max}=40^{\circ}$, $\nu=0.5$ on the TF, both in the thrust faulting regime. We calibrate the value of R_0 individually on each fault to ensure reasonable slip on both segments, using $R_0=0.14$ on the RSF and $R_0=0.41$ on the TF (and all other faults). We lower R_0 to 0.14 on the RSF to prevent slip from becoming too large after rupture transfer. In this simulation we also increase the frictional cohesion (C_0) near the surface on the TF to 5 MPa to better produce the smooth transition across the TF without obvious surface rupture. We decrease the frictional cohesion near the surface on the RSF to 2 MPa to better produce the sharp surface rupture across the RSF observed in the InSAR data (Figure 14). We find that there is only a very narrow range of parameters that both allow rupture propagation to the RSF but generate a reasonable slip magnitude on the RSF. We ultimately find an appropriate combination of parameters: $D_c=0.02$, $mu_s=0.52$, $mu_d=0.16$, $\alpha=0.7$.

This rupture, like Model 4, begins with largely unilateral rupture to the west. After about 10 seconds, the rupture reaches the intersection between the RSF and TF (Figure 11d) and soon after encounters increased static friction west of point \mathbf{U} (Figure 15). Here, the rupture almost stops but eventually begins to slip at the intersection between the RSF and TF. The rupture on the RSF slips slowly at first, then accelerates toward the surface of the RSF. Slip on the RSF has rake ranging between ~ 40 -60°, and slip on the TF has rake ranging between ~ 0 -30°. This period where the rupture encounters the intersection of the RSF and TF corresponds to the trough in the source time function expected from the teleseismic data at about 10 seconds (Okuwaki & Fan, 2022; Goldberg et al., 2022; Calais et al., 2022).

Several additional simulations which are not shown adjusted the location of 'point T' (Figure 12) where static friction increase begins, to better understand its relationship to rupture transfer, timing, and fit to the InSAR data. We find that when introducing an increase in μ_s on the TF further to the west, rupture extends further to the west before transferring to the RSF. This is inconsistent with the InSAR data which indicates that there is no subsurface rupture that far west. When the μ_s on the TF increases west of point \mathbf{T} , we find that the rupture transfers more quickly to the RSF, resulting in a better fit to the moment rate and better fit to the InSAR data. Even with these adjustments, there is still some disagreement with the InSAR data at the western edge of the TF, west of point X (Figure 14c and 13b). We find that it is difficult to produce the concentrated slip near the surface on the RSF which is observed in the InSAR data. This remaining discrepancy causes some misfit between the modeled surface deformation and the InSAR and GNSS data near the Ravine du Sud fault (Figure 14c, RMS=0.213 for A043, RMS=0.093 for D138). However, the simulated rupture from Model 5 has otherwise strong agreement with all observations: InSAR surface deformation, GNSS offsets, and source time function. It also produces all of the key characteristics of the earthquake: separation of strike slip and dip slip motion on two separate fault planes, rupture transfer to the RSF, and source time function peaks.

As in Model 3, the kinematically informed stress heterogeneities which are included in the initial stress state for Model 5 act to spatially concentrate slip, but do not ultimately control the spatial extent, overall magnitude of slip, or rupture transfer between faults. This is apparent when comparing the final slip distribution of Model 5 to an alternative Model 6 (Figure S3) which considers all of the complexity used in Model 5 but excludes kinematically informed stress heterogeneities and re-calibrates the R_0 value to mimic the same stress-strength balance as Model 5. Models 5 and 6 share similar slip extents, moment magnitudes, and both produce rupture transfer from the TF to RSF. However, there is some marginal loss of spatial complexity of the slip distribution in Model 6 which is apparent in Model 5. Model 5 on average has slightly better fits with the In-

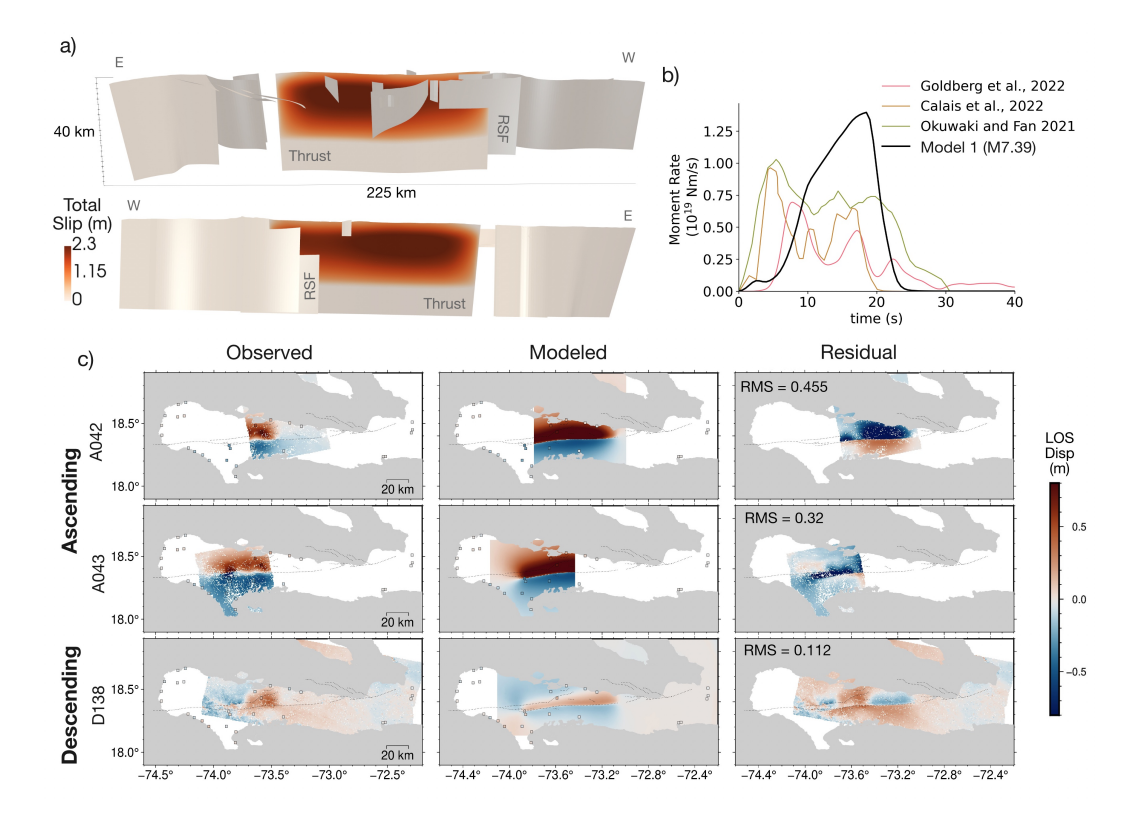


Figure 8. Summary of results from Model 1: Regional stresses in the thrust regime a) Final slip distribution. Slip is distributed evenly over the entire TF, no rupture transfer to the RSF; b) source time function comparison among Goldberg et al. (2022) (pink), Calais et al. (2022) (gold), Okuwaki and Fan (2022) (green) and this model (black). Overall rupture moment magnitude is too large and there are no distinct pulses, unlike the Goldberg et al. (2022) source time function; c) Observed InSAR data from ALOS-2 tracks A042, A043, an D138 compared with simulated LOS surface deformation data. Overall magnitude of surface deformation is too large, creating a large misfit in pattern and moment magnitude between the modeled deformation and observed deformation, seen as large residuals.

SAR observations. In this way, the dynamics of the event can be represented with or without kinematically-derived stresses. If one is concerned with matching the detailed slip features to better match the observed data, then these stress heterogeneities can be useful. For this reason, we include these stress heterogeneities in the preferred model (Model 5) but offer an alternative simulation that does not include the kinematically derived stresses to showcase a simpler solution that comes at some small cost of fit to the smaller scale deformation details and less agreement with the kinematic slip distribution (see supplemental section 3.1). The main result is therefore that a significant along-strike change in the regional stress field is necessary to produce the observed slip on the RSF in our fault geometry as well as some variation in along-strike dynamic parameters such as fault strength.

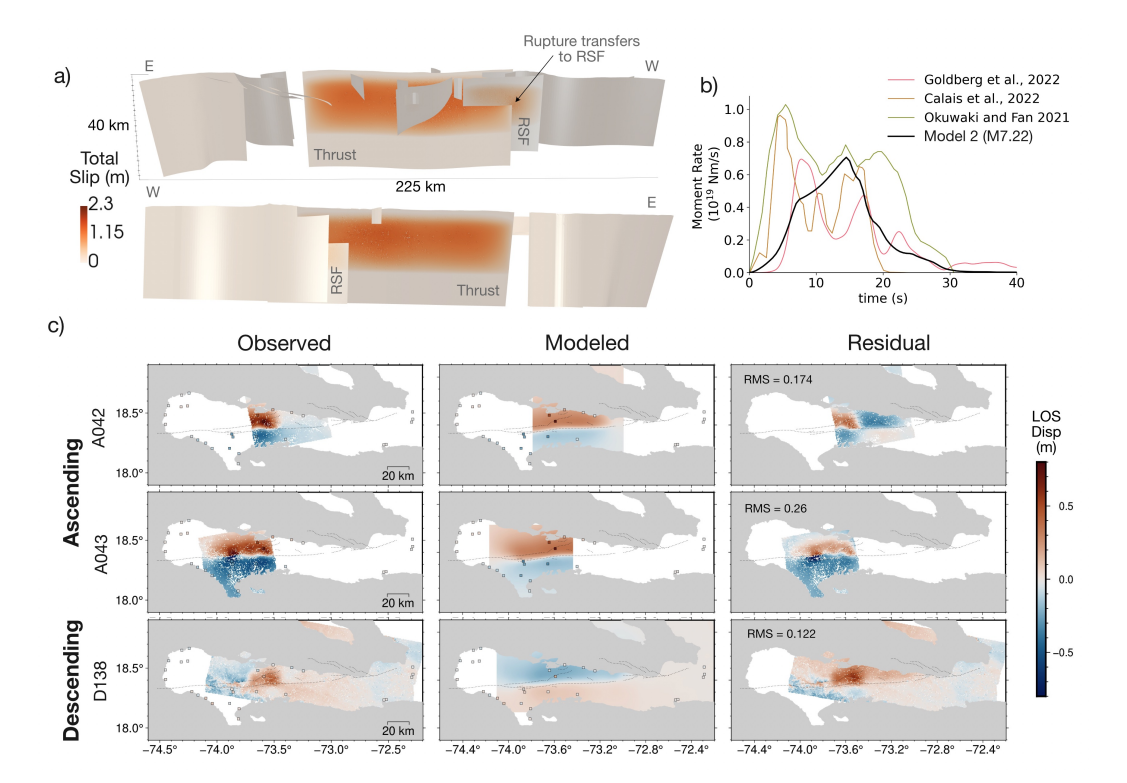


Figure 9. Summary of results from Model 2: regional stresses in the strike slip faulting regime: a) Final slip distribution for Model 2. Slip is distributed evenly over the entire TF and rupture has propagated to the RSF with significant slip; b) source time function comparison among Goldberg et al. (2022) (pink), Calais et al. (2022) (gold), Okuwaki and Fan (2022) (green) and this model (black). Overall rupture moment magnitude is captured but without distinct peaks, unlike the Goldberg et al. (2022) source time function; c) Observed InSAR comparison with simulated LOS surface deformation data. Amplitude of residuals is decreased with respect to Model 1, however there remains a strong misfit in the pattern between the modeled deformation and observed deformation. The descending pair (D138) shows negative deformation in the LOS direction of the observing satellite whereas we expect a lobe of positive deformation from strong thrust motion the TF as seen in the observed interferogram. This indicates the stress orientation plays a role in producing later slip on the RSF which contributes to creating a peak later in the source time function.

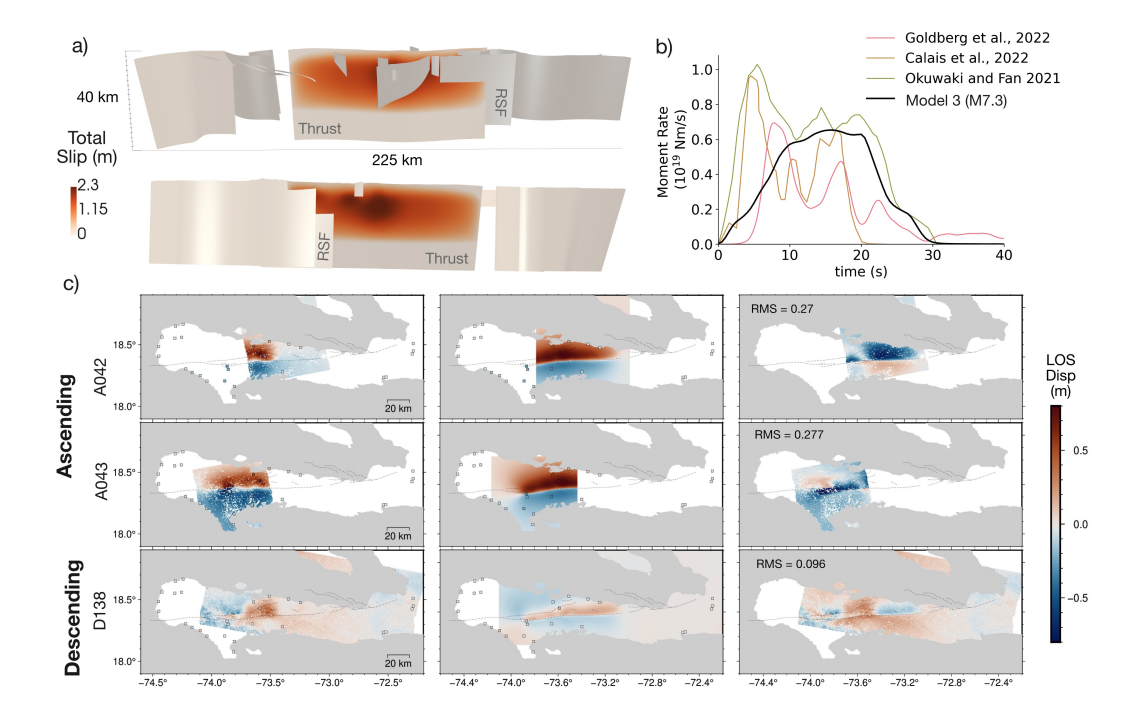


Figure 10. Summary of results from Model 3: Combined regional and Kinematically Informed Heterogeneous Stresses in the thrust regime a) Final slip distribution for Model 3. While slip still extends over the entire length of TF, slip concentrates near the center of the fault. There is no rupture transfer to the RSF; b) source time function comparison among Goldberg et al. (2022) (pink), Calais et al. (2022) (gold), Okuwaki and Fan (2022) (green) and this model (black). The peak of the source time function is roughly the right amplitude but there are no distinct peaks and the single peak is too wide; c) Observed InSAR data from ALOS-2 tracks A042, A043, an D138 compared with simulated LOS surface deformation data. Overall magnitude of surface deformation remains too large, but uplift, seen as a red lobe in the simulated track D138 data, is broadly matched. This indicates that concentrating the dip-slip motion in lateral extent is important for matching the InSAR pattern with dip-slip dominating strike-slip motion in the surface deformation.

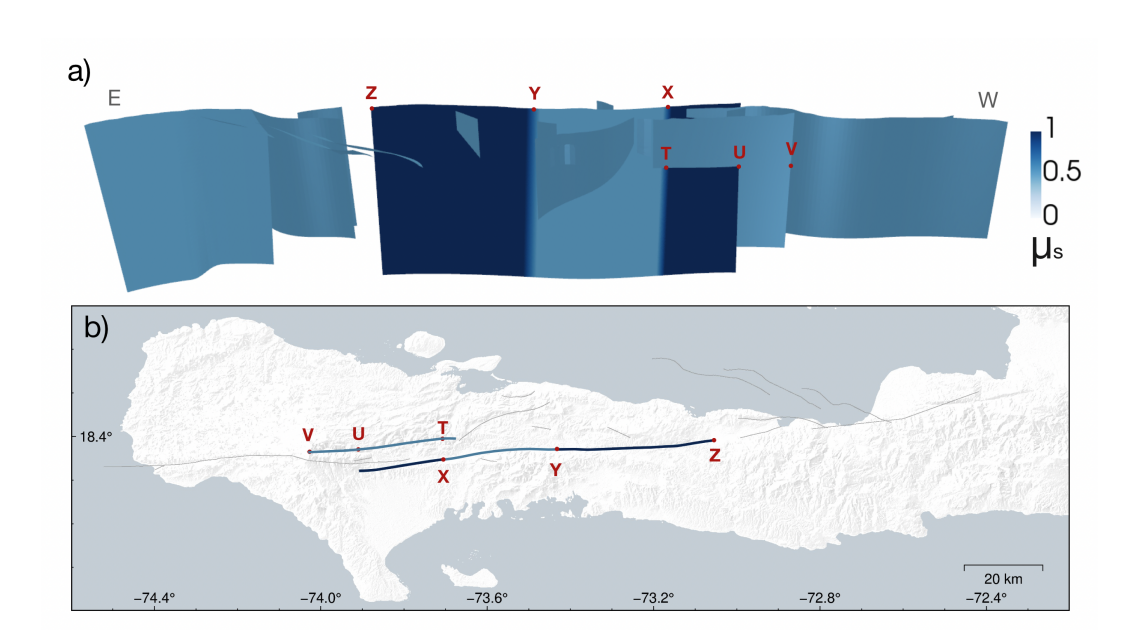


Figure 11. Variable static coefficient of friction on the fault surfaces. This distribution of μ_s is used in both Model 4 and Model 5. Points of interest T, U, V, X, Y, and Z are shown in red.

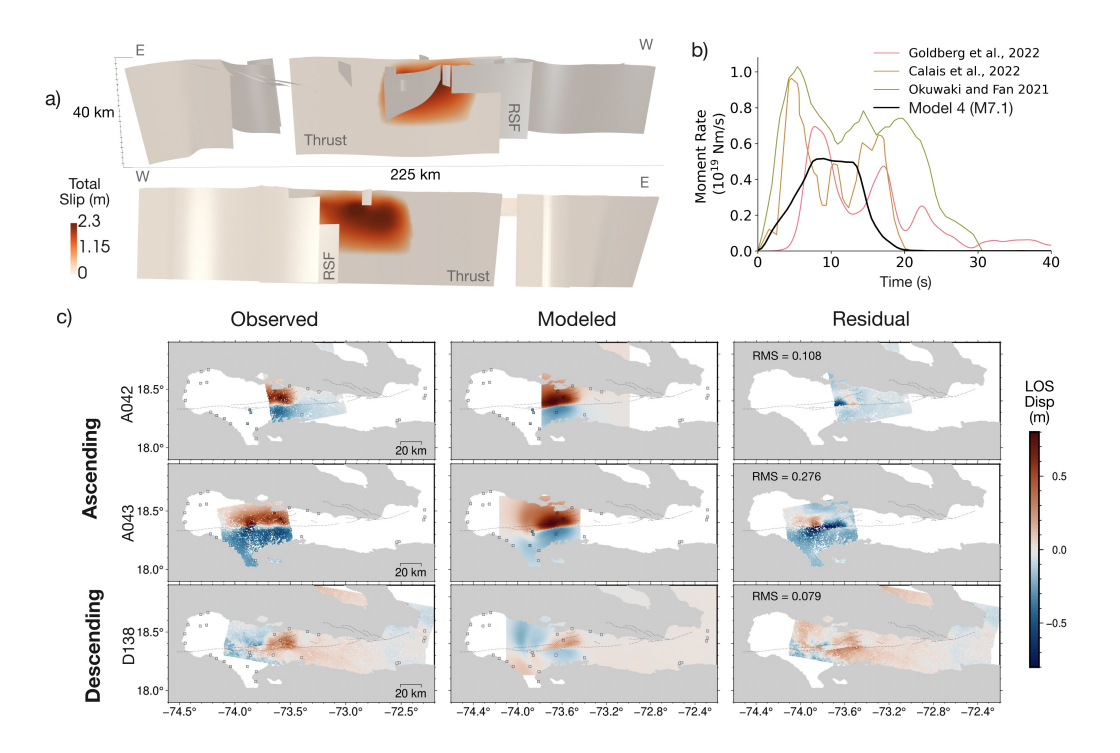


Figure 12. Summary of results from Model 4: combined regional and Kinematically Informed Heterogeneous stresses in the thrust faulting regime with fault strength variations: a) Final slip distribution for Model 4. Slip patches are more compact than in Model 2, but there is no rupture transfer and therefore no slip shown on the RSF; b) source time function comparison among Goldberg et al. (2022) (pink), Calais et al. (2022) (gold), Okuwaki and Fan (2022) (green) and this model (black). Overall moment magnitude is captured but there are no distinct peaks in the source time function, unlike the Goldberg et al. (2022) model; c) Observed InSAR comparison with simulated LOS surface deformation data. Modeled surface deformation data closely matches the observations in amplitude and pattern. In particular, the synthetic descending LOS deformation (D138) shows a lobe of positive deformation in the LOS direction of the observing satellite which agrees with the observed interferogram. This indicates that a limited rupture extent on TF contributes to matching the pattern of uplift.

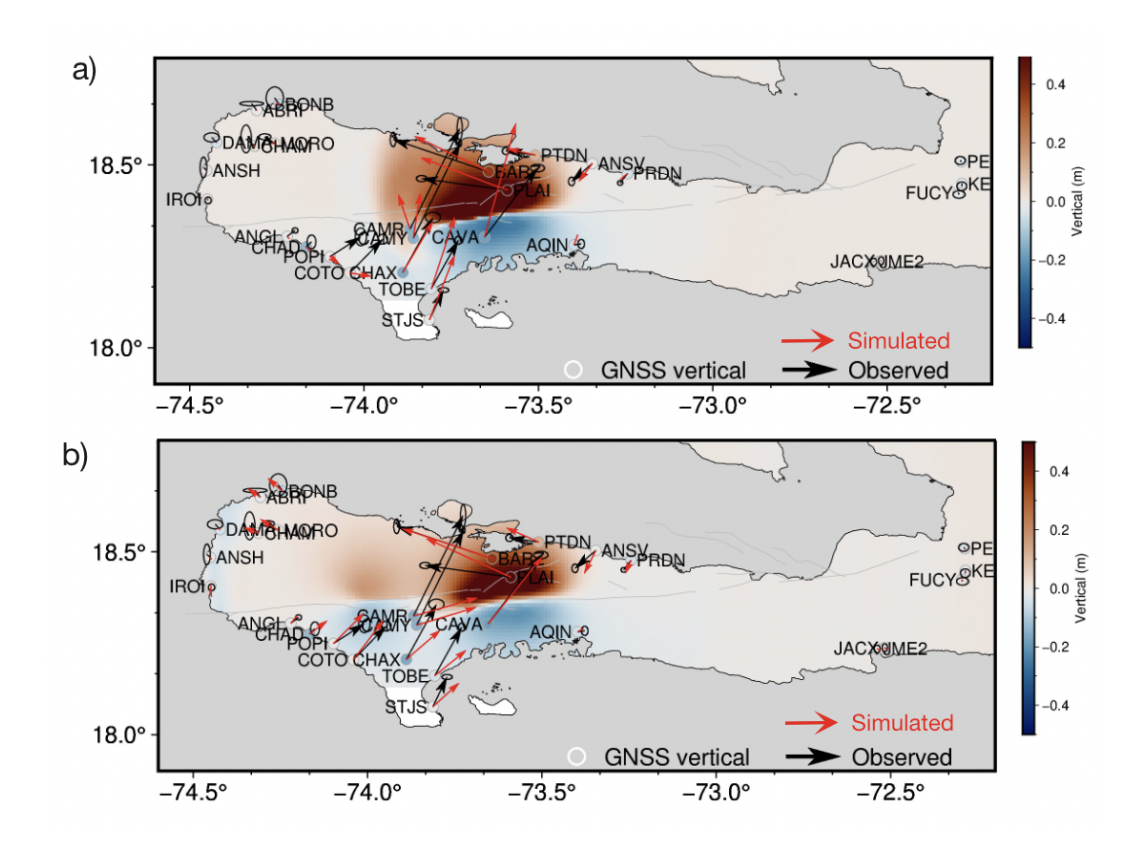


Figure 13. Comparison between observed GNSS coseismic offsets (horizontal deformation shown with black arrows, vertical deformation shown by color of circles) and simulated offsets (horizontal deformation shown with red arrows, vertical deformation shown as the background gridded red/blue data). a) Model 4 comparison; b) Model 5 comparison.

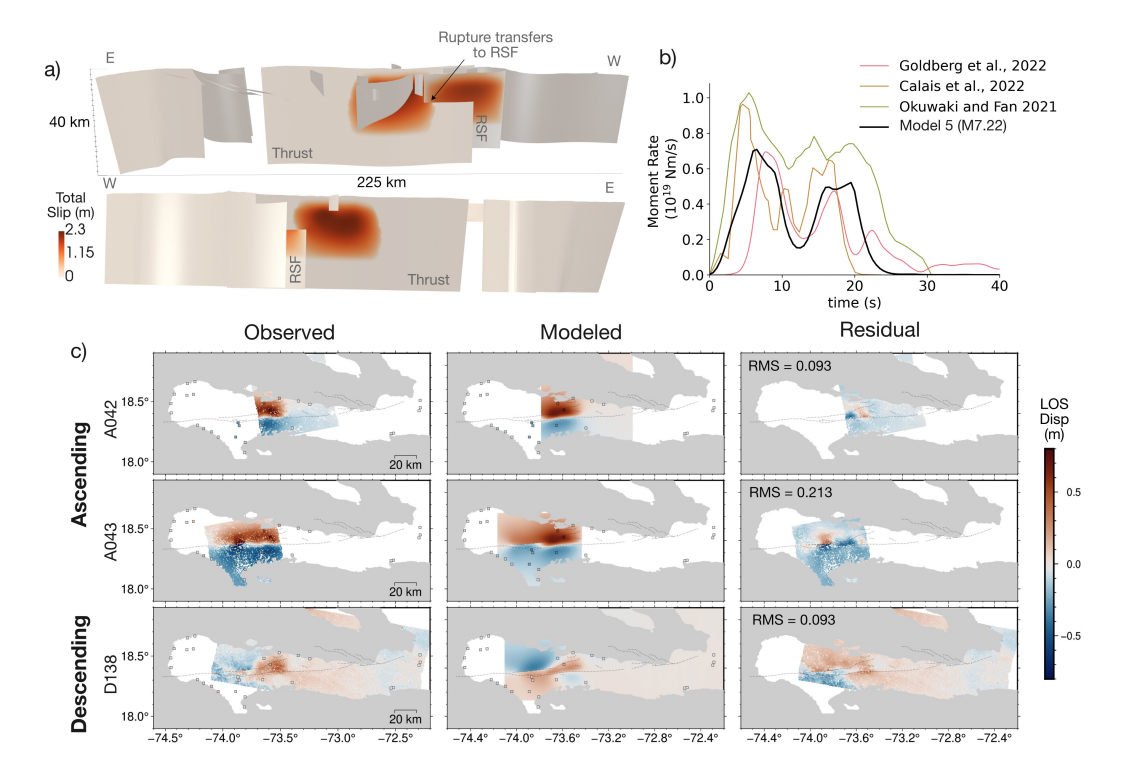


Figure 14. Summary of results from Model 5: Lateral variations in regional stresses combined with Kinematically Informed Heterogeneous stresses and fault strength variations: a) Final slip distribution for model 5. Slip patches concentrate compactly on the TF and RSF, where slip on the RSF indicates successful rupture transfer b) source time function comparison among Goldberg et al. (2022) (pink), Calais et al. (2022) (gold), Okuwaki and Fan (2022) (green) and this model (black), where there is good agreement in the moment magnitude and timing, and where the two distinct peaks in the source time function correspond to the rupture transfer from TF to RSF; c) Observed InSAR comparison with simulated LOS surface deformation data. Modeled surface deformation data closely matches the pattern and amplitude of the observations, with the synthetic descending LOS deformation (D138) showing the expected lobe of positive deformation in the LOS direction. The deformation now matches the InSAR deformation in the narrow region between the RSF and TF.

5 Discussion

5.1 Predictability of Rupture Dynamics

The simulations presented of the 2021 Haiti event illustrate important limitations on the ability to foresee even large scale rupture features of future earthquakes based on limited a priori tectonic knowledge. Changes in the representation of fault geometry as illustrated both by the introduction of fault strength barriers (Models 4 and 5, Figure 11) as well as the orientation of the fault planes relative to the regional stress shape and orientation (Figure 7) together controlled both the rupture extent and the direction of slip on the fault surfaces. In this study it was important to know the observed rupture extent and general slip characteristics of the earthquake in order to infer changes in geometry and regional stresses which ultimately controlled the simulated rupture. Without this post hoc knowledge, it would be nearly impossible to have foreseen the extent, slip distribution, and dynamics of the rupture. While this is unfortunate from a seismic

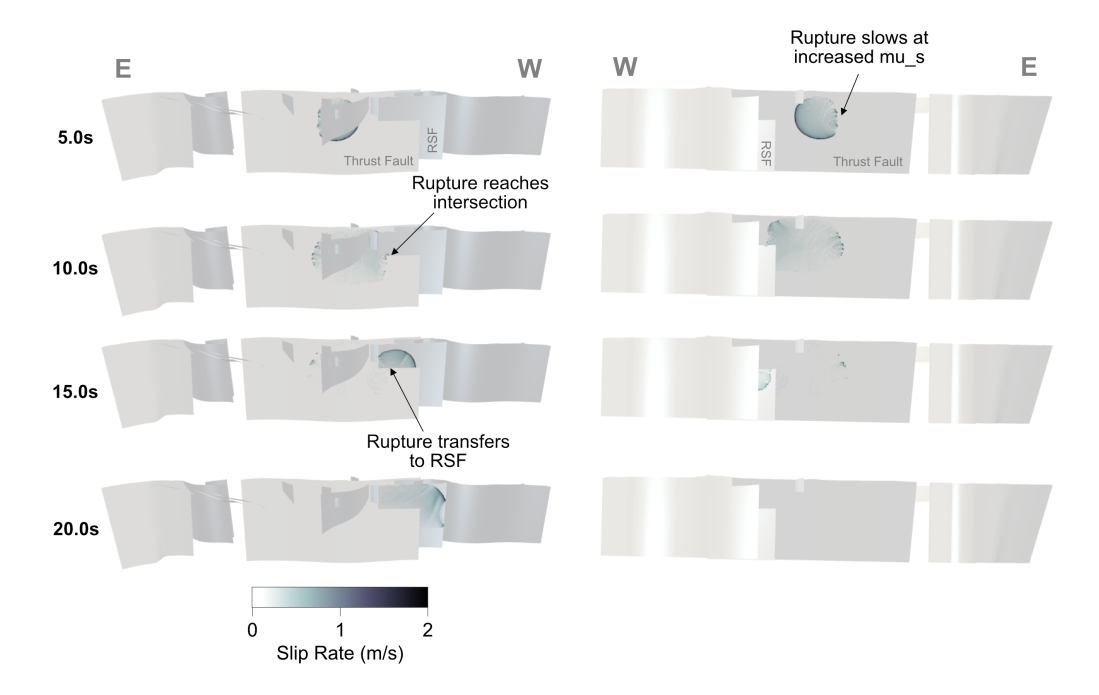


Figure 15. Snapshots of absolute slip velocity for Model 5. Left column shows a view from the north and right column shows a view from the south. Rupture nucleates on the TF, at 10 s reaches the intersection with the RSF where the slip velocity decreases before, at 15 sec, rupture transfers to the RSF and slip velocity increases as the rupture propagates upwards before terminating at around 20 sec.

hazard perspective, it is an important fundamental limitation in our model. At the same time, this result implies that improved characterization of fault geometry and regional stress fields may lead to improved hazard characterization. Broader scale observations like geodetic observations of interseismic strain accumulation and locking extents, studies of past seismicity and corresponding likely regions of slip deficit, as well as detailed study of existing fault geometries could all be used to better constrain the family of possible ruptures on this and other faults zones. Observational seismologists, geologists, and geodesists in this region are operating in a severely challenging field environment (S. Symithe, 2025), but our results highlight the importance of their continued work.

5.2 Interpretation of the Thrust Fault

One important unresolved question about the 2021 earthquake is the relationship of the Thrust Fault to the EPGF (Saint Fleur et al., 2020; Prentice et al., 2003). Several studies have supported the interpretation of a mature, largely vertical EPGF which hosts primarily strike slip motion over geologic timescales. Geodetic block modeling studies (e.g. Calais et al., 2023, Manaker et al., 2008, Symithe et al., 2014; 2015) also support largely strike slip motion on the EPGF. Decades of geological and geomorphologic studies of the Tiburon peninsula provide evidence for a well-expressed near-vertical strike slip EPGF (Prentice et al., 2003, Mann et al., 1995, Saint Fleur et al., 2020). One of the outstanding puzzles of this region is that there is so much evidence for a near-vertical, primarily strike-slip EPGF, yet the recent 2010 and 2021 earthquakes show that this fault system is not simply a strike slip fault system. Indeed, these events open the possibilities that the EPGF may be more complex and varied than past studies have shown and that surrounding faults may be participating meaningfully in seismic hazard generation. The fault system geometry has major implications for understanding how this margin accommodates transpression.

The Thrust Fault used in our model roughly follows the trace of the EPGF (Saint Fleur et al., 2020), and continues at depth dipping 66°N, constrained such that it roughly follows aftershock locations (Douilly et al., 2023). The fault is represented as a single, nearly planar feature as in Raimbault et al. (2023). The ability of Model 5 to match observations of the 2021 event suggests that the TF geometry with our proposed modifications represents one possible geometry. As more aftershock locations and relocations became available (Douilly et al., 2023), they suggested that at depth this fault is likely not planar but can instead be interpreted as two or three planes that more closely follow aftershock clusters. This kind of variation of fault strike could also terminate of limit the extent of fault rupture, which we produced by varying fault friction. There is also a small subset of aftershocks that lie in a vertical plane below the EPGF fault trace east of the rupture that may indicate the presence of a separate EPGF (Figure 1). In this conception, the vertical EPGF would produce the persistent topographic features observed and, over geologic time, would take up the motion of a larger earthquake.

It remains unclear if this north-dipping fault, whether comprised of a single planar segment or multiple segments, is itself the EPGF or a parallel strand running alongside the vertical EPGF. The possibility of two parallel faults with different dips has different implications for understanding the long-term accommodation of strain across the peninsula. Designing new meshed fault geometries would be an important undertaking for expanded dynamic rupture modeling experiments to help address these different hypotheses. This study serves as a guide for the level of detail and scope of simulations that could supplement such future studies.

The results of our modeling suggest that the TF geometry that we proposed is subject to transpressive regional stresses which are most closely approximated by a thrust-faulting stress regime with a stress shape ratio ν =0.5 on this fault. Recent GNSS work from Calais et al. (2023) proposed two possible block models in which shortening is ei-

ther accommodated almost entirely by the Jeremie-Malpasse thrust fault off the northshore of the Tiburon peninsula or an alternative model where compression and strike slip motion are both accommodated along the EPGF. Our model results support the interpretation that significant shortening is acting as far south as the mapped EPGF, as opposed to being entirely accommodated by offshore thrusts, like the Jeremie-Malpasse fault to the north (Calais et al., 2023).

Including significantly longer fault segments in the model than actually ruptured in the main earthquake led to several challenges in matching the observed behavior. However, it also led to a more in-depth understanding of the controls on fault rupture. For example, had we made the assumption in advance that the TF terminated at the start of the RSF then rupture would likely have transferred to the RSF without an investigation of the many factors that control that transfer.

5.3 Unruptured Miragoâne Segment

783

784

788

789

792

793

794

795

797

798

799

801

802

805

806

807

808

809

810

811

812

813

814

815

817

818

819

820

821

822

823

825

826

827

828

830

831

832

The Thrust Fault was designed to extend from Massif Macaya all the way to Lake Miragoâne (Figure 1) and dips 66°N. This distance is considerably longer than the extent of the known rupture from InSAR data (Figure 1b). From the Basin of L'Asile to Lake Miragoâne, we increase the static friction coefficient in Models 4 and 5 in order to terminate rupture where surface deformation becomes negligible in the InSAR data. Increasing μ_s or decreasing initial shear stresses locally to terminate rupture is a common approximation used in dynamic rupture modeling, particularly when using a LSW friction law, where there is no mechanism to account for velocity-strengthening rheology of the fault that may decelerate dynamic rupture (e.g. Galis et al., 2019). The segment of the EPGF between the 2010 and 2021 ruptures is puzzling because both earthquakes were estimated to have increased the Coulomb Failure Stress here (Calais et al., 2022; S. J. Symithe et al., 2013). Interestingly, the west and the east ends of this unruptured segment also slipped shallowly in the weeks following the 2010 and 2021 earthquakes, respectively (Yin et al., 2022; Wdowinski & Hong, 2012). It is critical to understand whether this segment is locked and highly hazardous, or whether it is accommodating strain differently than the surrounding segments.

One explanation could be that the the eastern edge of the 2021 rupture simply marks the end of the TF where it intersects with the vertical EPGF. This change in geometry could prevent the propagation of the rupture onto the unruptured segment. This interpretation is supported by the change from north-dipping to vertical clusters of aftershock seismicity east of the rupture (Douilly et al., 2023). A change in fault dip could also make rupture transfer less dynamically feasible, as we showed was the case for the rupture transfer between the north-dipping TF and vertically-dipping RSF, which would explain the eastern termination of the rupture. Another possibility is that the unruptured segment is relatively weak and, for example, creeping at depth such that there is little stress remaining to be released to continue the rupture. However, the GNSS velocity transects across the fault do not indicate interseismic creep (Calais et al., 2015), nor does recent interseismic InSAR analysis (Raimbault, 2023). A third possibility is that this segment ruptured most recently (i.e. 1770, see Hough et al., 2023) and stress has not yet recovered.

5.4 TF West of the 2021 Rupture

In Models 4 and 5, we increase the static coefficient of friction west of the rupture as seen in the InSAR. Increasing the static fault strength of this section was required to match the InSAR surface deformation field and GNSS coseismic offsets and matched the timing of the first trough in the modeled source time functions (Goldberg et al., 2022; Calais et al., 2022; Okuwaki & Fan, 2022). The dynamic rupture models demonstrated a need to increase the static strength of the west end of the TF that is parallel to the

RSF in order to match the observations. This suggests that, while at one point this may have been an active strand of the EPGFZ or part of a flower structure, it is either no longer active or the north-dipping TF ends before this section begins.

Here and for the east end of the TF, the change in frictional properties can be considered a proxy for fault characteristics or features that change that location. The change in characteristics means that segmentation is important, however as the two earthquakes in 2010 and 2021 showed, it cannot be easily interpreted from surface features in advance. This presents challenges for earthquake hazard estimates that include a recurrence model for characteristic earthquakes based on fault length (Wells & Coppersmith, 1994). A statistical approach that accounts for different potential rupture lengths (e.g. Field et al., 2014) is necessary.

5.5 Strain Partitioning at the EPGF

The oblique relative motion between the North American and Caribbean tectonic plates creates transpression across Hispaniola. However, there is ongoing debate about how that transpression is accommodated and partitioned among fault systems. While the Enriquillo-Plantain Garden Fault Zone (EPGFZ) has historically been understood to be a vertical fault accommodating only left lateral motion, recent geodetic work, recent re-examination of historical events, and oblique focal mechanisms in the recent 2010 and 2021 earthquakes supports the interpretation that significant crustal shortening and thrust faulting reaches as far south as the EPGF. The partitioning of strain across the region plays a critical role in our understanding or earthquake hazard and risk in Haiti (S. Symithe & Calais, 2016). Recent block modeling of GNSS data proposed two competing block models for this region, but the observations cannot easily distinguish between the two models (Calais et al., 2023).

The historical earthquakes in 1701, 1770, and 1860, were assumed to be strike slip earthquakes which occurred on the EPGF (Bakun et al., 2012). Some have used this to suggest a multi-rupture mode for this plate boundary which alternates between strike slip events on the EPGF and thrust events on secondary faults over the course of centuries (Wang et al., 2018). However, (Hough et al., 2023) recent re-examination of the 1770 and 1860 events, suggests that these events could have occurred on partially on oblique thrust faults (Hough et al., 2023; Martin & Hough, 2022). This, combined with the knowledge of the 2010 and 2021 events both initiating on north-dipping unmapped thrust faults, suggests that perhaps significant thrust motion is a typical mode of failure for this fault zone. Despite significant geologic field work and other geophysical data collection over the last several decades, there is still high uncertainty in the fault dip through much of the peninsula. Perhaps fault segmentation includes sections of vertical strike slip fault (like the unruptured section) while other sections prefer oblique thrusting. This work supports the interpretation of combined thrust and strike slip motion and adds the constraint that this implies variation in the stress tensor along the plate boundary.

6 Conclusions

ຂຂດ

3D dynamic rupture modeling experiments were used to test which conditions may have contributed to the complex 2021 $M_w7.2$ Haiti earthquake rupture. We developed a highly complex fault geometry which included two main coseismic fault surfaces: a north-dipping Thrust Fault (TF) and a near-vertical Ravine du Sud Fault (RSF), as well as a detailed network of surrounding fault segments that allowed potential rupture over a much larger extent than was observed. The dynamic rupture models were tested against the following observations and characteristics: $M_w7.2$ moment magnitude, a multi-peak source time function, rupture transfer to the RSF, and spatial separation of dip slip and strike slip motion. This characteristic separation of dip slip and strike slip motion is ob-

served in the InSAR deformation pattern and confirmed by GNSS where vertical motion dominated over left lateral motion in the LOS direction.

Results indicate that regional stress shape and orientation were key influences on both the orientation of slip (rake) and the transfer of dynamic rupture from the TF to the RSF. Regional stress with orientation $SH_{max}=40^{\circ}$ and $\nu=0.5$ produced shear stress resolved on the TF that best aligned with the surface deformation observations. However, a dynamic rupture model using this simple description of regional stress (Model 1) did not produce the observed slip on the RSF, which suggested that a more complex system was required. While stress heterogeneities localized the simulated slip in closer agreement with the observed surface deformation pattern, they did not impact the lateral extent of rupture or the rupture transfer to the RSF. Changing the assumed orientation of the stress tensor and the stress shape ratio between the RSF and TF faults was required to produce transfer of the rupture to the RSF and to produce shear stresses on the RSF oriented in agreement with the observed rake.

Along-strike variations in fault friction on the TF were key to focusing the slip to the observed geographic patches and producing narrow, distinct peaks in the source time function. The change in frictional properties can be considered a proxy for fault characteristics or features that changed at that location, for example a change in orientation or termination of the fault. The change in along-strike characteristics means that segmentation is important, however as the two earthquakes in 2010 and 2021 showed, it cannot be easily interpreted from surface features in advance. In fact, the segmentation proposed in Saint Fleur et al. (2020) does not represent conditions that can lead to a dynamic rupture model that produces the observed characteristics.

Combining regional stress changes with along strike variations in fault friction created a major slip patch on the TF along with dynamic rupture transfer to the RSF with the right timing to match the source time functions. This simulation (Model 5) best fit all of the observational datasets. These results assume the dynamic rupture of a thrust fault with 66°N dip. However, this does not preclude the existence of a parallel vertical EPGF, nor does it test any variations in the assumed rupture geometry. Future dynamic rupture modeling efforts may be used to explore how variations in the defined fault rupture geometry would impact the dynamic rupture evolution.

These simulations imply that the regional stress field and the detailed fault geometry can both act as primary controls of slip extent, distribution, and rupture dynamics. Given the sensitivity to fault geometry, more work is needed to identify a comprehensive set of fault segments which may contribute to the accommodation of regional tectonics. Ideally, such a databse would estimate different probabilities of rupturing and include secondary faults that have been observed to respond to tectonic and co-seismic loading (Yin et al., 2022). Recent efforts to map and categorize surrounding faults (Calais et al., 2023; Saint Fleur et al., 2020, 2024) and monitor their microseismic activity (Calais et al., 2022; Douilly et al., 2023) will contribute to these ends.

7 Open Research

All data needed to produce the simulations described here are made available via an openly available Zenodo dataset (Yin et al., 2024). All dynamic rupture simulations were performed using SeisSol (Breuer et al., 2014; Gabriel et al., 2025). We use SeisSol, commit 60aedc8c (master branch on June 17, 2024). Instructions for downloading, installing, and running the code are available in the SeisSol documentation, including instructions on setting up and running simulations as well as a Docker container and Jupyter notebooks with quickstart containerized installations and introductory materials. Example problems and model configuration files are also provided in the documentation, many of which reproduce the SCEC 3D Dynamic Rupture benchmark problems (Harris

et al., 2009). Figures are produced using Generic Mapping Tools (GMT), (Wessel et al., 2019)

8 Declaration of Competing Interests

The authors declare no competing interests.

Acknowledgments

932 933

934

936

939

940

943

944

948

949

950

951

952

953

956

957

961

963

964

965

967

968

969

971

972

975

976

977

We thank the Associate Editor and two anonymous reviewers for their thorough and insightful review of this work, which we believe improved the manuscript and underlying work significantly.

We thank the operators and hosts of the Ayiti-Séismes earthquake monitoring network at Bureau des Mines, Faculté des Sciences, Laboratoire URGéo, Université d'état d'Haïti, Ecole Normale Supérieur, and Laboratoire Géoazur for providing aftershock locations and making them free and openly available. We thank ESA for the rapid acquisition and distribution of Sentinel-1 data. We thank JAXA for access to ALOS-1 and ALOS-2 data.

This collaboration was supported by Geo-INQUIRE, a project funded by the European Commission under project number 101058518 within the HORIZON-INFRA-2021-SERV-01 call (https://www.geo-inquire.eu/copyright/). Computing resources were provided by the Institute of Geophysics of LMU Munich and the Gauss Centre for Supercomputing (LRZ, project pn49ha) on the supercomputer SuperMUC-NG.

HZY acknowledges support by National Aeronautics and Space Administration (NASA), through the Future Investigators in NASA Earth and Space Science and Technology (FINESST) program (grant No. 80NSSC22K1533).

MM and AAG acknowledge additional support by Horizon Europe (grant No. 101093038, 101058129, and 101058518), NSF (grant No. EAR-2225286, EAR-2121568, OAC-2139536, OAC-2311208), and NASA (grant No. 80NSSC20K0495).

We gratefully acknowledge Jeremy Wong, Thomas Ulrich, and Jeena Yun for many helpful discussions related to SeisSol configurations and model setups. We also benefited greatly from discussions with Steeve Symithe and Eric Calais about the tectonic context, and conversations with Bryan Raimbault about the GNSS data and previous inversion results.

References

- Aki, K., & Richards, P. G. (1980). Quantitative seismology: Theory and methods. San Francisco: W. H. Freeman.
- Ando, R., & Kaneko, Y. (2018). Dynamic Rupture Simulation Reproduces Spontaneous Multifault Rupture and Arrest During the 2016 $M_{\rm w}$ 7.9 Kaikoura Earthquake. Geophysical Research Letters, 45(23). doi: 10.1029/2018GL080550
- Andrews, D. J. (1976). Rupture propagation with finite stress in antiplane strain. *Journal of Geophysical Research*, 81(20), 3575–3582. doi: 10.1029/JB081i020p03575
- Aochi, H. (2003). The 1999 Izmit, Turkey, Earthquake: Nonplanar Fault Structure, Dynamic Rupture Process, and Strong Ground Motion. *Bulletin of the Seismological Society of America*, 93(3), 1249–1266. doi: 10.1785/0120020167
- Aochi, H., & Ulrich, T. (2015). A Probable Earthquake Scenario near Istanbul Determined from Dynamic Simulations. Bulletin of the Seismological Society of America, 105(3), 1468–1475. doi: 10.1785/0120140283
- Bakun, W. H., Flores, C. H., & Ten Brink, U. S. (2012). Significant Earthquakes on

the Enriquillo Fault System, Hispaniola, 1500-2010: Implications for Seismic
Hazard. Bulletin of the Seismological Society of America, 102(1), 18–30. doi:
10.1785/0120110077

aga

- Bizzarri, A., & Cocco, M. (2003). Slip-weakening behavior during the propagation of dynamic ruptures obeying rate- and state-dependent friction laws. *Journal of Geophysical Research: Solid Earth*, 108(B8), 2002JB002198. doi: 10.1029/2002JB002198
- Breuer, A., Heinecke, A., Rettenberger, S., Bader, M., Gabriel, A.-A., & Pelties, C. (2014). Sustained Petascale Performance of Seismic Simulations with SeisSol on SuperMUC. In J. M. Kunkel, T. Ludwig, & H. W. Meuer (Eds.), Supercomputing (Vol. 8488, pp. 1–18). Cham: Springer International Publishing. doi: 10.1007/978-3-319-07518-1_1
- Calais, E., Freed, A., Mattioli, G., Amelung, F., Jónsson, S., Jansma, P., ... Momplaisir, R. (2010). Transpressional rupture of an unmapped fault during the 2010 Haiti earthquake. *Nature Geoscience*, 3(11), 794–799. doi: 10.1038/ngeo992
- Calais, E., Symithe, S., Mercier de Lépinay, B., & Prépetit, C. (2015). Plate boundary segmentation in the northeastern Caribbean from geodetic measurements and Neogene geological observations. Comptes Rendus. Géoscience, 348(1), 42–51. doi: 10.1016/j.crte.2015.10.007
- Calais, E., Symithe, S., Monfret, T., Delouis, B., Lomax, A., Courboulex, F., ... Meng, L. (2022). Citizen seismology helps decipher the 2021 Haiti earthquake. *Science*, 376(6590), 283–287. doi: 10.1126/science.abn1045
- Calais, E., Symithe, S. J., & de Lépinay, B. M. (2023). Strain Partitioning within the Caribbean–North America Transform Plate Boundary in Southern Haiti, Tectonic and Hazard Implications. Bulletin of the Seismological Society of America, 113(1), 131–142. doi: 10.1785/0120220121
- Das, S., & Aki, K. (1977). Fault plane with barriers: A versatile earth-quake model. *Journal of Geophysical Research*, 82(36), 5658–5670. doi: 10.1029/JB082i036p05658
- DeMets, C., Jansma, P. E., Mattioli, G. S., Dixon, T. H., Farina, F., Bilham, R., . . . Mann, P. (2000). GPS geodetic constraints on Caribbean-North America Plate Motion. *Geophysical Research Letters*, 27(3), 437–440. doi: 10.1029/1999GL005436
- Douilly, R., Aochi, H., Calais, E., & Freed, A. M. (2015). Three-dimensional dynamic rupture simulations across interacting faults: The M_w 7.0, 2010, Haiti earthquake. Journal of Geophysical Research: Solid Earth, 120(2), 1108–1128. doi: 10.1002/2014JB011595
- Douilly, R., Haase, J. S., Ellsworth, W. L., Bouin, M.-P., Calais, E., Symithe, S. J., . . . Hough, S. E. (2013). Crustal Structure and Fault Geometry of the 2010 Haiti Earthquake from Temporary Seismometer Deployments.

 Bulletin of the Seismological Society of America, 103(4), 2305–2325. doi: 10.1785/0120120303
- Douilly, R., Mavroeidis, G. P., & Calais, E. (2017). Simulation of broad-band strong ground motion for a hypothetical Mw 7.1 earthquake on the Enriquillo Fault in Haiti. *Geophysical Journal International*, 211(1), 400–417. doi: 10.1093/gji/ggx312
- Douilly, R., Paul, S., Monfret, T., Deschamps, A., Ambrois, D., Symithe, S. J., ... Chèze, J. (2023). Rupture Segmentation of the 14 August 2021 Mw 7.2 Nippes, Haiti, Earthquake Using Aftershock Relocation from a Local Seismic Deployment. Bulletin of the Seismological Society of America, 113(1), 58–72. doi: 10.1785/0120220128
- Dumbser, M., & Käser, M. (2006). An arbitrary high-order discontinuous Galerkin method for elastic waves on unstructured meshes II. The three-dimensional isotropic case. *Geophysical Journal International*, 167(1), 319–336. doi:

```
10.1111/j.1365-246X.2006.03120.x
```

- Farr, T. G., Rosen, P. A., Caro, E., Crippen, R., Duren, R., Hensley, S., ... Alsdorf, D. (2007). The Shuttle Radar Topography Mission. *Reviews of Geophysics*, 45(2), 2005RG000183. doi: 10.1029/2005RG000183
- Field, E. H., Arrowsmith, R. J., Biasi, G. P., Bird, P., Dawson, T. E., Felzer, K. R., ... Zeng, Y. (2014). Uniform California Earthquake Rupture Forecast, Version 3 (UCERF3)—The Time-Independent Model. Bulletin of the Seismological Society of America, 104(3), 1122–1180. doi: 10.1785/0120130164
- Gabriel, A.-A., Kurapati, V., Niu, Z., Schliwa, N., Schneller, D., Ulrich, T., ... Bader, M. (2025). SeisSol: June 17, 2024 release (commit 60aedc8c) [Software]. Zenodo. Retrieved from https://doi.org/10.5281/zenodo.4672483
- Gabriel, A.-A., Ulrich, T., Marchandon, M., Biemiller, J., & Rekoske, J. (2023). 3D Dynamic Rupture Modeling of the 6 February 2023, Kahramanmaraş, Turkey Mw 7.8 and 7.7 Earthquake Doublet Using Early Observations. The Seismic Record, 3(4), 342–356. doi: 10.1785/0320230028
- Galis, M., Ampuero, J.-P., Mai, P. M., & Kristek, J. (2019). Initiation and arrest of earthquake ruptures due to elongated overstressed regions. *Geophysical Journal International*, 217(3), 1783–1797. doi: 10.1093/gji/ggz086
- Garagash, D. I. (2021). Fracture mechanics of rate-and-state faults and fluid injection induced slip. *Philosophical Transactions of the Royal Society A: Mathematical, Physical and Engineering Sciences*, 379(2196), 20200129. doi: 10.1098/rsta.2020.0129
- Glehman, J., Gabriel, A.-A., Ulrich, T., Ramos, M., Huang, Y., & Lindsey, E. (2024). Partial ruptures governed by the complex interplay between geodetic slip deficit, rigidity, and pore fluid pressure in 3D Cascadia dynamic rupture simulations. doi: 10.31223/X5GH66
- Goldberg, D. E., Koch, P., Melgar, D., Riquelme, S., & Yeck, W. L. (2022). Beyond the Teleseism: Introducing Regional Seismic and Geodetic Data into Routine USGS Finite-Fault Modeling. Seismological Research Letters, 93(6), 3308–3323. doi: 10.1785/0220220047
- Harris, R. A., Barall, M., Aagaard, B., Ma, S., Roten, D., Olsen, K., ... Dalguer, L. (2018). A Suite of Exercises for Verifying Dynamic Earthquake Rupture Codes. Seismological Research Letters, 89(3), 1146–1162. doi: 10.1785/0220170222
- Harris, R. A., Barall, M., Andrews, D. J., Duan, B., Ma, S., Dunham, E. M., . . . Abrahamson, N. (2011). Verifying a Computational Method for Predicting Extreme Ground Motion. Seismological Research Letters, 82(5), 638–644. doi: 10.1785/gssrl.82.5.638
- Harris, R. A., Barall, M., Archuleta, R., Dunham, E., Aagaard, B., Ampuero, J. P., ... Templeton, E. (2009). The SCEC/USGS Dynamic Earthquake Rupture Code Verification Exercise. Seismological Research Letters, 80(1), 119–126. doi: 10.1785/gssrl.80.1.119
- Harris, R. A., & Day, S. M. (1999). Dynamic 3D simulations of earthquakes on En Echelon Faults. *Geophysical Research Letters*, 26(14), 2089–2092. doi: 10.1029/1999GL900377
- Hayek, J. N., Marchandon, M., Li, D., Pousse-Beltran, L., Hollingsworth, J., Li, T., & Gabriel, A.-A. (2024). Non-Typical Supershear Rupture: Fault Heterogeneity and Segmentation Govern Unilateral Supershear and Cascading Multi-Fault Rupture in the 2021 Mw7.4 Maduo Earthquake. Geophysical Research Letters, 51(20), e2024GL110128. doi: 10.1029/2024GL110128
- Heidbach, O., Rajabi, M., Cui, X., Fuchs, K., Müller, B., Reinecker, J., ...
 Zoback, M. (2018). The World Stress Map database release 2016:
 Crustal stress pattern across scales. *Tectonophysics*, 744, 484–498. doi: 10.1016/j.tecto.2018.07.007
- Heinecke, A., Breuer, A., Rettenberger, S., Bader, M., Gabriel, A.-A., Pelties, C., ... Dubey, P. (2014). Petascale High Order Dynamic Rupture Earthquake

Simulations on Heterogeneous Supercomputers. In SC14: International Conference for High Performance Computing, Networking, Storage and Analysis (pp. 3–14). New Orleans, LA, USA: IEEE. doi: 10.1109/SC.2014.6

- Hough, S. E., Martin, S. S., Symithe, S. J., & Briggs, R. (2023). Rupture Scenarios for the 3 June 1770 Haiti Earthquake. *Bulletin of the Seismological Society of America*, 113(1), 157–185. doi: 10.1785/0120220108
- Ida, Y. (1972). Cohesive force across the tip of a longitudinal-shear crack and Griffith's specific surface energy. *Journal of Geophysical Research*, 77(20), 3796–3805. doi: 10.1029/JB077i020p03796
- Jia, Z., Jin, Z., Marchandon, M., Ulrich, T., Gabriel, A.-A., Fan, W., . . . Fialko, Y. (2023). The complex dynamics of the 2023 Kahramanmaraş, Turkey, $M_{\rm w}$ 7.8-7.7 earthquake doublet. Science, 381 (6661), 985–990. doi: 10.1126/science.adi0685
- Kaneko, Y., Lapusta, N., & Ampuero, J.-P. (2008). Spectral element modeling of spontaneous earthquake rupture on rate and state faults: Effect of velocitystrengthening friction at shallow depths. Journal of Geophysical Research: Solid Earth, 113(B9), 2007JB005553. doi: 10.1029/2007JB005553
- Krenz, L., Uphoff, C., Ulrich, T., Gabriel, A.-A., Abrahams, L. S., Dunham, E. M.,
 & Bader, M. (2021). 3D acoustic-elastic coupling with gravity: The dynamics of the 2018 Palu, Sulawesi earthquake and tsunami. In Proceedings of the International Conference for High Performance Computing, Networking, Storage and Analysis (pp. 1–14). St. Louis Missouri: ACM. doi: 10.1145/3458817.3476173
- Li, Z., & Wang, T. (2023). Coseismic and Early Postseismic Slip of the 2021 Mw 7.2 Nippes, Haiti, Earthquake: Transpressional Rupture of a Nonplanar Dipping Fault System. Seismological Research Letters, 94(6), 2595–2608. doi: 10.1785/0220230160
- Ma, S., Custódio, S., Archuleta, R. J., & Liu, P. (2008). Dynamic modeling of the 2004 M $_{\rm w}$ 6.0 Parkfield, California, earthquake. Journal of Geophysical Research: Solid Earth, 113(B2), 2007JB005216. doi: 10.1029/2007JB005216
- Madariaga, R. (1976). Dynamics of an expanding circular fault. Bulletin of the Seismological Society of America, 66(3), 639–666. doi: 10.1785/BSSA0660030639
- Madden, E. H., Ulrich, T., & Gabriel, A.-A. (2022). The State of Pore Fluid Pressure and 3-D Megathrust Earthquake Dynamics. *Journal of Geophysical Research: Solid Earth*, 127(4), e2021JB023382. doi: 10.1029/2021JB023382
- Manaker, D. M., Calais, E., Freed, A. M., Ali, S. T., Przybylski, P., Mattioli, G., . . . de Chabalier, J. B. (2008). Interseismic Plate coupling and strain partitioning in the Northeastern Caribbean. *Geophysical Journal International*, 174(3), 889–903. doi: 10.1111/j.1365-246X.2008.03819.x
- Mann, P., Taylor, F., Edwards, R., & Ku, T.-L. (1995). Actively evolving microplate formation by oblique collision and sideways motion along strike-slip faults: An example from the northeastern Caribbean plate margin. Tectonophysics, 246(1-3), 1-69. doi: 10.1016/0040-1951(94)00268-E
- Martin, S. S., & Hough, S. E. (2022). The 8 April 1860 Jour de Pâques Earthquake Sequence in Southern Haiti. Bulletin of the Seismological Society of America, 112(5), 2468–2486. doi: 10.1785/0120220016
- Maurer, J., Dutta, R., Vernon, A., & Vajedian, S. (2022). Complex rupture and triggered aseismic creep during the August 14, 2021 Haiti earthquake from satellite geodesy (Preprint). Geodesy. doi: 10.1002/essoar.10510731.1
- Mercier de Lépinay, B., Deschamps, A., Klingelhoefer, F., Mazabraud, Y., Delouis,
 B., Clouard, V., ... St-Louis, M. (2011). The 2010 Haiti earthquake: A
 complex fault pattern constrained by seismologic and tectonic observations:
 THE 2010 HAITI EARTHQUAKE FAULT PATTERN. Geophysical Research
 Letters, 38(22), n/a-n/a. doi: 10.1029/2011GL049799
 - Miyatake, T. (1992). Dynamic rupture processes of inland earthquakes in Japan

weak and strong asperities. Geophysical Research Letters, 19(10), 1041–1044. doi: 10.1029/92GL01046

- National Geophysical Data Center. (1972). Global Significant Earthquake Database. NOAA National Centers for Environmental Information. doi: 10.7289/V5TD9V7K
- Nielsen, S. B., Carlson, J. M., & Olsen, K. B. (2000). Influence of friction and fault geometry on earthquake rupture. Journal of Geophysical Research: Solid Earth, 105(B3), 6069–6088. doi: 10.1029/1999JB900350
- Okuwaki, R., & Fan, W. (2022). Oblique Convergence Causes Both Thrust and Strike-Slip Ruptures During the 2021 M 7.2 Haiti Earthquake. *Geophysical Research Letters*, 49(2), e2021GL096373. doi: 10.1029/2021GL096373
- Palgunadi, K. H., Gabriel, A.-A., Ulrich, T., López-Comino, J. Á., & Mai, P. M.
 (2020). Dynamic Fault Interaction during a Fluid-Injection-Induced Earthquake: The 2017 Mw 5.5 Pohang Event. Bulletin of the Seismological Society of America, 110(5), 2328–2349. doi: 10.1785/0120200106
- Prentice, C. S., Mann, P., Crone, A. J., Gold, R. D., Hudnut, K. W., Briggs, R. W., ... Jean, P. (2010). Seismic hazard of the Enriquillo–Plantain Garden fault in Haiti inferred from palaeoseismology. *Nature Geoscience*, 3(11), 789–793. doi: 10.1038/ngeo991
- Prentice, C. S., Mann, P., Peña, L. R., & Burr, G. (2003). Slip rate and earthquake recurrence along the central Septentrional fault, North American—Caribbean plate boundary, Dominican Republic. *Journal of Geophysical Research: Solid Earth*, 108(B3), 2001JB000442. doi: 10.1029/2001JB000442
- Raimbault, B. (2023). Space-based seismotectonic of Hispaniola Island (Unpublished doctoral dissertation). Université Paris sciences et lettres.
- Raimbault, B., Jolivet, R., Calais, E., Symithe, S., Fukushima, Y., & Dubernet,
 P. (2023). Rupture Geometry and Slip Distribution of the Mw 7.2 Nippes
 Earthquake, Haiti, From Space Geodetic Data. Geochemistry, Geophysics,
 Geosystems, 24(4), e2022GC010752. doi: 10.1029/2022GC010752
- Ramos, M. D., Thakur, P., Huang, Y., Harris, R. A., & Ryan, K. J. (2022). Working with Dynamic Earthquake Rupture Models: A Practical Guide. Seismological Research Letters, 93(4), 2096–2110. doi: 10.1785/0220220022
- Rice, J. R. (1992). Chapter 20 Fault Stress States, Pore Pressure Distributions, and the Weakness of the San Andreas Fault. In *International Geophysics* (Vol. 51, pp. 475–503). Elsevier. doi: 10.1016/S0074-6142(08)62835-1
- Saint Fleur, N., Dessable, J. E., Saint-Preux, G., Calais, É., Feuillet, N., Boisson, D., ... Klinger, Y. (2024). Tectonic, Topographic, Geologic, and Hydroclimatic Influence on Crack Formation During the 2021 Haiti Earthquake. Geochemistry, Geophysics, Geosystems, 25 (7), e2023GC011255. doi: 10.1029/2023GC011255
- Saint Fleur, N., Feuillet, N., Grandin, R., Jacques, E., Weil-Accardo, J., & Klinger, Y. (2015). Seismotectonics of southern Haiti: A new faulting model for the 12 January 2010 M 7.0 earthquake. Geophysical Research Letters, 42(23). doi: 10.1002/2015GL065505
- Saint Fleur, N., Klinger, Y., & Feuillet, N. (2020). Detailed map, displacement, paleoseismology, and segmentation of the Enriquillo-Plantain Garden Fault in Haiti. *Tectonophysics*, 778, 228368. doi: 10.1016/j.tecto.2020.228368
- Simpson, R. W. (1997). Quantifying Anderson's fault types. *Journal of Geophysical Research: Solid Earth*, 102(B8), 17909–17919. doi: 10.1029/97JB01274
- Suppe, J. (2014). Fluid overpressures and strength of the sedimentary upper crust. Journal of Structural Geology, 69, 481–492. doi: 10.1016/j.jsg.2014.07.009
- Symithe, S. (2025). Geosciences in Dangerous Area: The Case of Haiti. In *Seismological Society of America Annual Meeting*. Baltimore, MD: Seismological Society of America.
- Symithe, S., & Calais, E. (2016). Present-day shortening in Southern Haiti from GPS measurements and implications for seismic hazard. *Tectonophysics*, 679,

117-124. doi: 10.1016/j.tecto.2016.04.034

- Symithe, S., Calais, E., de Chabalier, J. B., Robertson, R., & Higgins, M. (2015). Current block motions and strain accumulation on active faults in the Caribbean. *Journal of Geophysical Research: Solid Earth*, 120(5), 3748–3774. doi: 10.1002/2014JB011779
- Symithe, S. J., Calais, E., Haase, J. S., Freed, A. M., & Douilly, R. (2013). Coseismic Slip Distribution of the 2010 M 7.0 Haiti Earthquake and Resulting Stress Changes on Regional Faults. *Bulletin of the Seismological Society of America*, 103(4), 2326–2343. doi: 10.1785/0120120306
- Taufiqurrahman, T., Gabriel, A.-A., Li, D., Ulrich, T., Li, B., Carena, S., ...

 Gallovič, F. (2023). Dynamics, interactions and delays of the 2019 Ridge-crest rupture sequence.

 Nature, 618 (7964), 308–315. doi: 10.1038/s41586-023-05985-x
- Tinti, E., Casarotti, E., Ulrich, T., Taufiqurrahman, T., Li, D., & Gabriel, A.-A. (2021). Constraining families of dynamic models using geological, geodetic and strong ground motion data: The Mw 6.5, October 30th, 2016, Norcia earthquake, Italy. Earth and Planetary Science Letters, 576, 117237. doi: 10.1016/j.epsl.2021.117237
- Tinti, E., Fukuyama, E., Piatanesi, A., & Cocco, M. (2005). A Kinematic Source-Time Function Compatible with Earthquake Dynamics. Bulletin of the Seismological Society of America, 95(4), 1211–1223. doi: 10.1785/0120040177
- Ulrich, T., Gabriel, A.-A., Ampuero, J.-P., & Xu, W. (2019). Dynamic viability of the 2016 Mw 7.8 Kaikōura earthquake cascade on weak crustal faults. *Nature Communications*, 10(1), 1213. doi: 10.1038/s41467-019-09125-w
- Uphoff, C., Rettenberger, S., Bader, M., Madden, E. H., Ulrich, T., Wollherr, S., & Gabriel, A.-A. (2017). Extreme scale multi-physics simulations of the tsunamigenic 2004 sumatra megathrust earthquake. In *Proceedings of the International Conference for High Performance Computing, Networking, Storage and Analysis* (pp. 1–16). Denver Colorado: ACM. doi: 10.1145/3126908.3126948
- Wang, J., Mann, P., & Stewart, R. R. (2018). Late Holocene Structural Style and Seismicity of Highly Transpressional Faults in Southern Haiti. *Tectonics*, 37(10), 3834–3852. doi: 10.1029/2017TC004920
- Wdowinski, S., & Hong, S.-H. (2012). Postseismic Deformation Following the 2010 Haiti Earthquake: Time-dependent Surface Subsidence Induced by Groundwater Flow in Response to a Sudden Uplift. In *Fringe 2011 Workshop'*, *Frascati*, *Italy*, 19–23 September 2011. ESA.
- Wells, D. L., & Coppersmith, K. J. (1994). New empirical relationships among magnitude, rupture length, rupture width, rupture area, and surface displacement. Bulletin of the Seismological Society of America, 84 (4), 974–1002. doi: 10.1785/BSSA0840040974
- Wen, G., Li, X., Zhao, Y., Zhang, Y., Xu, C., & Zheng, Y. (2023). Kinematic Rupture Process and Its Implication of a Thrust and Strike-Slip Multi-Fault during the 2021 Haiti Earthquake. Remote Sensing, 15(7), 1730. doi: 10.3390/rs15071730
- Wessel, P., Luis, J. F., Uieda, L., Scharroo, R., Wobbe, F., Smith, W. H. F., & Tian, D. (2019). The Generic Mapping Tools (Version 6) [Software]. *Geochemistry*, *Geophysics*, *Geosystems*, 20(11), 5556–5564. doi: 10.1029/2019GC008515
- Wollherr, S., Gabriel, A.-A., & Mai, P. M. (2019). Landers 1992 "Reloaded": Integrative Dynamic Earthquake Rupture Modeling. *Journal of Geophysical Research: Solid Earth*, 124(7), 6666–6702. doi: 10.1029/2018JB016355
- Yang, H., Yao, S., He, B., & Newman, A. V. (2019). Earthquake rupture dependence on hypocentral location along the Nicoya Peninsula subduction megathrust. Earth and Planetary Science Letters, 520, 10–17. doi: 10.1016/j.epsl.2019.05.030
 - Yin, H. Z., Marchandon, M., Haase, J. S., Gabriel, A.-A., & Douilly, R. (2024).

1253	3D dynamic rupture modeling of the 2021 Haiti earthquake used to con-
1254	strain stress conditions and fault system complexity [Data Set].
1255	10.5281/zenodo.14368531
1256	Yin, H. Z., Xu, X., Haase, J. S., Douilly, R., Sandwell, D. T., & Mercier de Lepinay,
1257	B. (2022). Surface Deformation Surrounding the 2021 Mw 7.2 Haiti Earth-
1258	quake Illuminated by InSAR Observations. The Bulletin of the Seismological
1259	Society of America, 113, 41–57. doi: 10.1785/0120220109